

Wide Field of View Imaging System Design:

A Computational Imaging Approach

By

Donald B. T. Kilgus

A Masters Report Submitted to the Faculty of the

COLLEGE OF OPTICAL SCIENCES

In Partial Fulfillment of the Requirements for the Degree of

MASTER OF SCIENCE

In the Graduate College

THE UNIVERSITY OF ARIZONA

2016

Table of Contents

Abstract	2
Chapter 1 Introduction	3
Chapter 2 Optical Design.....	8
2.1. First order design requirements.....	8
2.2. Candidate lens design forms	10
2.2.1. Double Gauss	10
2.2.2. Simple Landscape Lens with Asphere at Stop.....	13
2.3. Simplification of a well-corrected WFOV lens: The Retrofocus Lens.....	18
2.3.1. Lens design process and merit function design:	20
2.3.2. Baseline design	21
2.3.3. Design of the field-invariant retrofocus lens.....	30
Chapter 3 Digital Image Restoration	45
3.1. Linear Wiener filter design	45
3.2. Image simulation.....	48
3.3. Digital image restoration and analysis	50
Chapter 4 Conclusion and Future Work	54
References.....	55

Abstract

Applying principles of computational imaging, we explore the design space of conventional wide field-of-view (FOV) imaging systems for opportunities to simplify the lens optical design, with the ultimate goal of reducing system complexity/cost. Specifically, by deliberately engineering an aberrated but field-invariant lens optical transfer function (OTF), we can achieve nearly diffraction-limited system performance using digital image restoration with fewer optical elements than a traditional, purely optical diffraction-limited lens design. A diffraction-limited baseline lens design and a second design with two fewer lens elements are modeled and their full-system imaging performance is simulated. Equivalent performance between the two systems, each with three aspheric surfaces, is achieved by optimizing the computational imaging system with a simpler lens, which has an asymmetric profile for the aspheric surface at the aperture stop. By using an end-to-end system model, we quantify the noise sensitivity and establish noise limits of the computational imaging system.

Chapter 1 Introduction

While the field of lens design is relatively mature, and design forms of a vast range of sizes, shapes, and functions have been invented and extensively optimized, the optical components of a modern imaging system tend to dominate the system cost and size. Conversely, the rapid advances in digital electronics in recent decades have yielded tremendous increases in the amount of computing power readily available at a device level at relatively low cost that can be brought to bear for real-time sensing and image processing in electronic imaging systems. This juxtaposition of states of the art in optics and digital electronics has motivated researchers to find ways to shift the functionality burden of an imager away from the optics and toward the electronics by jointly engineering and optimizing these apparently disparate system elements. This field, in which optical design, electronic sensing, and digital processing elements of a system are designed in concert to achieve an optimal set of system requirements, is known as computational imaging.

The inception of computational imaging is primarily attributed to Dowski and Cathey, who in 1995[1] published work wherein they integrated elements from the fields of radar and Fourier optics to conceive a method to significantly extend the depth of focus of an imaging system by adding a cubic phase modulation (cubic pm) mask at the aperture stop of the lens. The effect of this phase mask on the raw image – an effect referred to as wavefront coding (WFC) or point spread function (PSF) engineering – was to introduce substantial blur, but to do so in a fashion that rendered it largely depth-invariant. The asymmetric cubic pm phase function leads to an intensity PSF which is also asymmetric, with significant side lobes. The back half, i.e. post-measurement section, of the system design was designed to invoke a digital image restoration algorithm to correct for the blur by digitally deconvolving the blurred optical PSF via frequency domain filtering. The Fourier transform of the PSF is the OTF, and its modulus – the modulation transfer function (MTF) – is the primary means of illustrating the effects of the PSF and the deconvolution filter. These concepts are illustrated in Figure 1.

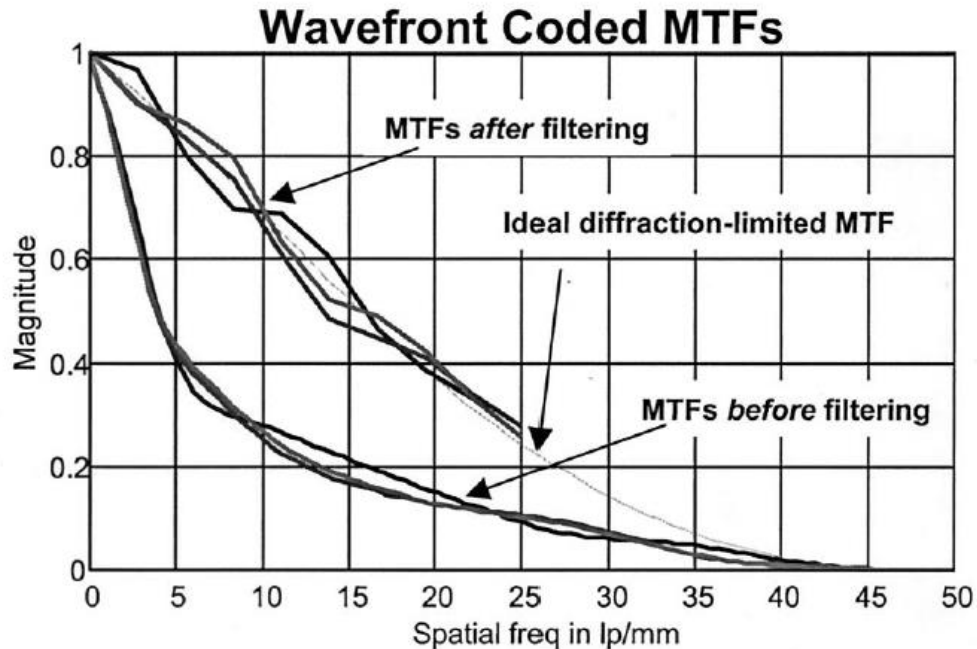


Figure 1 - WFC raw MTF and restored MTF curves, compared with the diffraction limit (adapted from [2]).

As is well-known from the digital image restoration field [2], the major tradeoff associated with such techniques is the amplification of measurement or sensor noise. Thus the degree to which this extended depth of focus (EDoF) technique is generally applicable depends among other things on how noisy the images are and how tolerant the application is of noise gain. However, this systems approach to EDoF provides significant advantages over purely optical solutions such as stopping down the aperture to create a slower $f/\#$, or aperture apodization – notably the preservation of overall optical intensity which these approaches lack.

It did not take long for the applicability of EDoF by wavefront coding to be explored by researchers, as its potential to profoundly impact systems designs was realized. The original inventors expanded on its principles by introducing the concept of an expanded “focus budget” [2], which could be used for purposes other than simply extending the focal depth of an existing imaging system. For systems already employing digital image restoration, they pointed out that cubic WFC enabled a depth-insensitive reconstruction filter, and (unlike defocus PSFs) an MTF without zeroes, which would lead to irretrievable

information loss in a system with linear post-processing. Subsequently they further generalized the applicability by illustrating how incorporating the technology could reduce the overall system complexity by simplifying the optics [4].

Subsequent work in computational imaging branched in several directions, with several teams recognizing that the longstanding imager design approach of first designing optics to deliver the best image possible, and separately designing the electronics and processing, was no longer optimal. These researchers developed new, holistic modeling methodologies and design tools which could facilitate efforts to design and optimize imaging systems from end to end [5][6][7][8]. Several other groups also explored the extensibility of wavefront coding to aspherics – whether phase masks or existing optical surfaces – beyond simple cubic functions. Generalization of the focus-extending benefit to higher order odd aspheric terms was theoretically established and experimentally demonstrated in several instances [9][10][11][12]. The common denominator in all of these cases was the need for the aspheric shape to include odd terms, thus breaking the traditional radial symmetry of conventional spherical and aspheric optics. A notable exception to the asymmetric asphere rule was from the research done by Dorronsoro et al [13] to explore the introduction of asymmetric phase error by misadjusting an otherwise symmetric optical element. This technique – successfully demonstrated in a longwave IR imager – has the potential to save substantially on the costs of optics fabrication and testing when compared to asymmetric aspheric elements.

A seemingly orthogonal research direction emanating from the early wavefront coding work was performed by researchers who sought applicability of computational imaging to tasks and applications well beyond EDoF. Notable areas of such work – among the many which exist – include applying computational principles to simplify superresolution multiframe imaging systems [14] and grayscale imaging systems [15]. In other cases, such as [16], computational imaging methods are helping to enable remarkable new imaging modalities.

In particular relevance to the present topic, computational imaging has also been brought to bear to increase the FOV in non-traditional ways: Nakamura et al [17] presented simulations of a wide FOV system utilizing spherical arrays of image sensors and compound eye lenses, while Treeaporn et al [18] modeled and demonstrated a liquid crystal-based approach to optical multiplexing which achieved a 3X increase in the FOV of a static imager. While neither of these unconventional approaches to FOV extension is foundational to the work described here, there has been computational imaging work published which is more closely related. Returning to the concept of a focus budget in the context of wavefront coding for EDoF, the exploitation of an increased budget for mitigation of focus-related aberrations, including field curvature (FC), astigmatism, and axial chromatic aberration, was suggested early on by Cathey and Dowski [2]. Notable work toward specifically leveraging EDoF for alleviation of axial chromatic aberration has been done [19][20], and, while not utilizing EDoF, very relevant work by Sahin et al [21] demonstrates the value of using computational imaging to remove lateral chromatic aberration in wide FOV color imagers, thus relieving the optics of a key design constraint. There has, however, been comparatively little published work on utilizing wavefront coding specifically for field curvature or astigmatism mitigation, or for using computational imaging methods for simplification of conventional wide FOV imager design more generally. The motivation was clearly called out by Shafer [22] as he showed the dramatic performance gains achievable for a given optical complexity when a curved image surface is allowed, although his indication of applicability was toward curved image sensors rather than pupil phase engineering. The subject was also directly broached by Thompson and Rolland [22] in 2014, who illustrated how with EDoF – specifically via phase mask trefoil Zernike aspheric terms in this case – curved focal surfaces can be fully encompassed within an EDoF volume. However, this work was not significantly generalized to address the usefulness of EDoF for simplifying the optical designs of wide FOV systems.

In the present work, opportunities are sought to leverage computational imaging in conventional wide FOV imager design in order to significantly simplify the optics. Our premise is that if a lens design

can be achieved which delivers a PSF which is aberrated in such a way that, while significantly larger than the diffraction limit, it is substantially field-invariant, then the corresponding OTF will be restorable with digital filtering to an effectively diffraction-limited system transfer function (STF).

A traditional lens design which is polychromatically diffraction-limited over a 60°-70° field-of-view (FOV) may require 6 to 10 lens elements, depending on aperture size and whether aspheric surfaces are employed. Our objective is to achieve - in a digital-optical imaging system - similar overall performance over that FOV to a diffraction limited baseline lens, but with reduced optical complexity by pursuing specifically aberrated lens designs that enable full digital restoration. The most basic image restoration approaches – which we rely upon here to support applicability to real-time imaging systems – use digital frequency domain techniques involving linear, direct filtering (non-iterative) of the OTF to produce a restored STF, and these filters rely on the OTF being similar over the entire FOV. Thus the simpler lens we pursue must have a substantially field-invariant OTF, and we will generally refer to it as the “field-invariant” lens. The Wiener filter (WF) provides optimum linear filtering to balance OTF restoration with minimization of noise amplification when low-cost, real-time filtering is needed [18][20]. The Wiener filter design takes into account the expected signal to noise ratio of the imagery in order to optimally roll off the gain at higher spatial frequencies, where otherwise noise gain would be high.

Chapter 2 of this report details the optical design effort pursued and summarizes performance and design details of two lenses – a baseline diffraction limited lens and field-invariant lens – which are proposed for analysis. In Chapter 3, image simulations performed in Zemax OpticStudio™ [24] and MATLAB® [25] are described, along with results of modeling and analysis of image restorations with and without noise. Chapter 4 concludes the report with a summary of findings and suggestions for further work.

Chapter 2 Optical Design

We develop first order requirements for our optical system, which are set forth in Table 1, and proceed to evaluate different lens design forms. Targeting a medium complexity design with no more than approximately 6 elements, we approached the problem from one of two directions depending on the lens form starting point: (1) adding complexity to simple lenses, or (2) judiciously reducing more complex lenses. In both cases the methodology is the same: (a) identify a starting lens which is comprised only of spherical elements, (b) construct a merit function in Zemax which reflects our requirements, (c) pursue design modifications and optimizations with reasonable spherical elements, (d) add standard (even polynomial) aspherics when all-spherical designs reach their limits, and (e) invoke asymmetric aspherics if needed to ultimately achieve the design goals. The rationale for this approach is that with the advent of modern CNC optical grinding and polishing equipment, aspheric surfaces on glass elements are achievable in medium to low volumes with reasonable economy, and thus introduction of aspherics to a design is generally preferable to adding more spherical elements – particularly because increasing element count also drives mechanical component and assembly complexities. There is also published work suggesting that aspheres are generally needed to achieve high-performance wide-angle lens design, and the main question is how many of them are required, and can their surface sag departures from best fit spheres be minimized [26]. CNC equipment is also capable of grinding and polishing asymmetric aspheres, although costs might be expected to be higher than with symmetric aspheres [26][27], especially with respect to interferometric testing.

2.1. First order design requirements

The work described here is not targeted to a specific application. However, in order to define a framework on which to evaluate the different design approaches, we choose the 35mm camera format – a well-known space of lens design forms – as our basis. This implies an image height of

approximately 22mm (half diagonal of 24x36mm image format). We further specify a moderately wide full-FOV goal of 64°, which then requires a lens focal length of:

$$EFL = H_{img} / \tan \theta_{\frac{1}{2}} = \frac{22mm}{\tan 32^\circ} \cong 33mm \quad (1)$$

To attain diffraction limited performance with a wide angle and high numerical aperture (NA) in a traditional lens design, substantial complexity and path length would likely be required [28]. To limit the complexity of the lens design (less than ~8 elements), a moderately fast lens speed of f/5.6 is chosen. The complete set of requirements is listed in Table 1:

PARAMETER	VALUE
Effective Focal Length	33mm
F/number	5.6
Field-of-View	64°
Design conjugate	Infinity
Back Focal Distance	42mm
Total Track Length	120mm
Analysis Wavelengths	486, 588, and 656nm

Table 1- First order lens design specifications

Other noteworthy requirements include having a physically realizable aperture stop. To elaborate, this means that during the design process it was recognized that, unless specifically constrained, the pupil aberrations could become so great that the paraxial stop position and full-field stop position could end up far apart, which would have the implication of allowing in large amounts of uncontrolled light that would not be represented in the modeled lens performance. Additionally, distortion was explicitly ignored. Given the assumption that this is a computational imaging system, it is further assumed that real time correction of distortion in digital processing (based on an as-built

imager calibration) is a reasonable expectation. It should be noted, however, that distortion correction is not within the scope of this work. Lastly it is noted that lens performance is generally evaluated at the paraxial image plane to ensure the centering of the image in the depth of focus.

2.2.Candidate lens design forms

Three design forms were initially evaluated for this work: (a) the double Gauss lens, (b) the plano-convex landscape lens, and (c) the retrofocus (also known as reverse telephoto) lens. The retrofocus is a standard lens type for wide-field photography and is known to be well-suited for fields of view and apertures in the vicinity of our requirements, whereas we are at the periphery of the applicability for the double Gauss [29]. The plano-convex landscape lens is just that: a single element lens and a well-placed aperture stop. While not directly suitable for our requirements, it is an intriguing starting point because the only monochromatic, non-stigmatic aberration it exhibits is spherical aberration [30], which is straightforward to correct. As described in the following sections, the three forms were explored, and the retrofocus lens was ultimately pursued in depth toward our design goals.

2.2.1. Double Gauss

A Double Gauss is a classic lens design form which requires minimal complexity to achieve diffraction limit over a 30° - 45° FOV. An initial question was whether it might be practical to start with an existing Double Gauss lens which is well-corrected over a 47° FOV [31] and stretch the FOV to 64° while forcing the aberrations to be field-independent. To reduce the experimental work in early phases, this lens was first simplified to a single glass type (SK16) and then re-optimized around a single wavelength of 587nm. Extending the FOV to 64° and optimizing for MTF invariance over the field (Figure 2) was achievable monochromatically over low to mid spatial frequencies, but there was larger MTF separation among the fields at higher frequencies (Figure 3), and zeroes well below the cutoff frequency for off-axis. Study of the OPD curves of this configuration (Figure 4) reveals a

significant amount of “stress” entering the design, meaning that 4th and 6th order aberrations are becoming substantial as they seek to balance one another in the optimization. The Double Gauss form is known for being limited by oblique spherical aberration (SA) at wide angles [32], which is wavefront error that is proportional to the fourth power of aperture and quadratic with field. It appears from the OPD plots that oblique SA is in fact beginning to dominate at this FOV, and other aberrations such as astigmatism and 4th order SA are being driven up to balance it, which is inducing the design stress. Since this lens was having difficulty meeting the requirements monochromatically, and achromatization was expected to drive substantially higher complexity, we made the decision to suspend work on the double Gauss as a preferred design form.

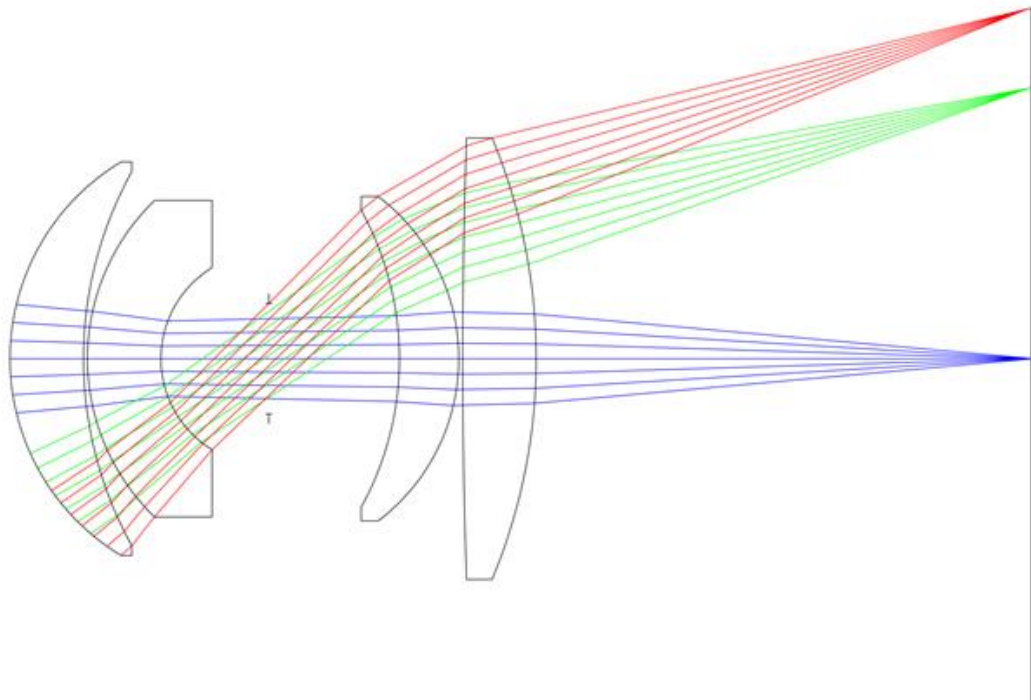


Figure 2 - Double Gauss lens monochromatically optimized for f/5.6 and 64-degree FOV

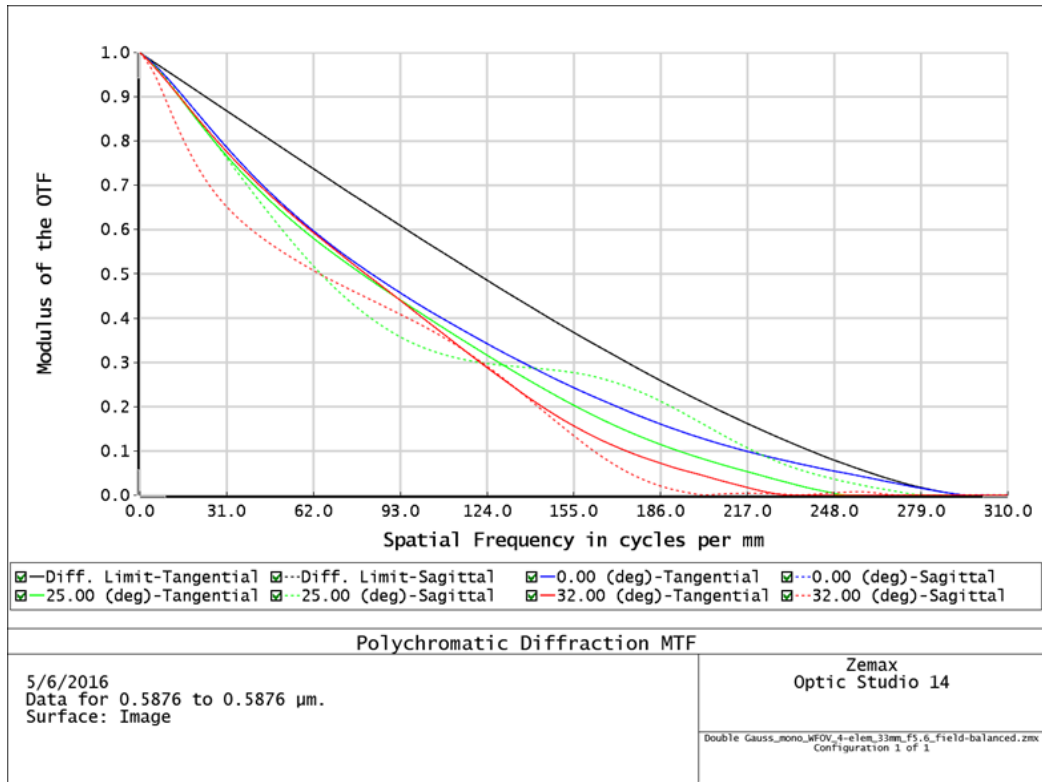


Figure 3 - MTF curves for monochromatically optimized Double Gauss lens

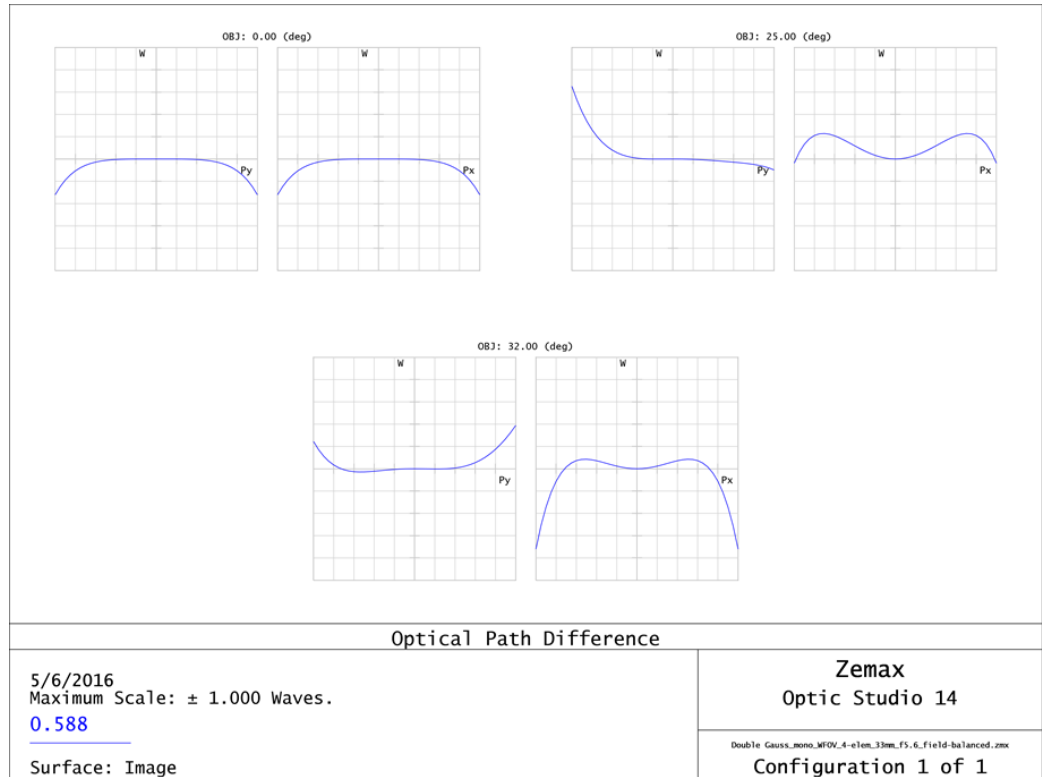


Figure 4 - Monochromatic OPD plots for Double Gauss lens

2.2.2. Simple Landscape Lens with Asphere at Stop

By optimization of stop position in front of a plano-convex lens, fourth order coma and astigmatism are nulled, enabling a simple, wide-FOV landscape lens that is free of these aberrations. Substantial spherical aberration (SA) and field curvature (FC) aberrations remain, but since SA is known to be fully correctable at with an asphere located at the stop, and since FC is a focus-related aberration which could ultimately be mitigated via EDoF wavefront coding, this design approach holds promise. Our goal will be to achieve good correction on a curved focal surface, with the intent that we will primarily be left with FC, which is only defocus vs. field angle. In the initial probing of this form we restrict the analysis initially to be monochromatic at 587nm. Note that the simplicity of this design form necessitates violating the 42mm minimum BFD requirement, as the back focal distance is approximately equal to the effective focal length, which was specified at 33mm.

This baseline design is fourth order coma- and astigmatism-free due to the stop and lens positions and the planar first surface. The field curvature dominance is highly evident even in the ray-trace diagram, and we can see in Figure 6 that even though FC dominates, SA is also severe (as expected).

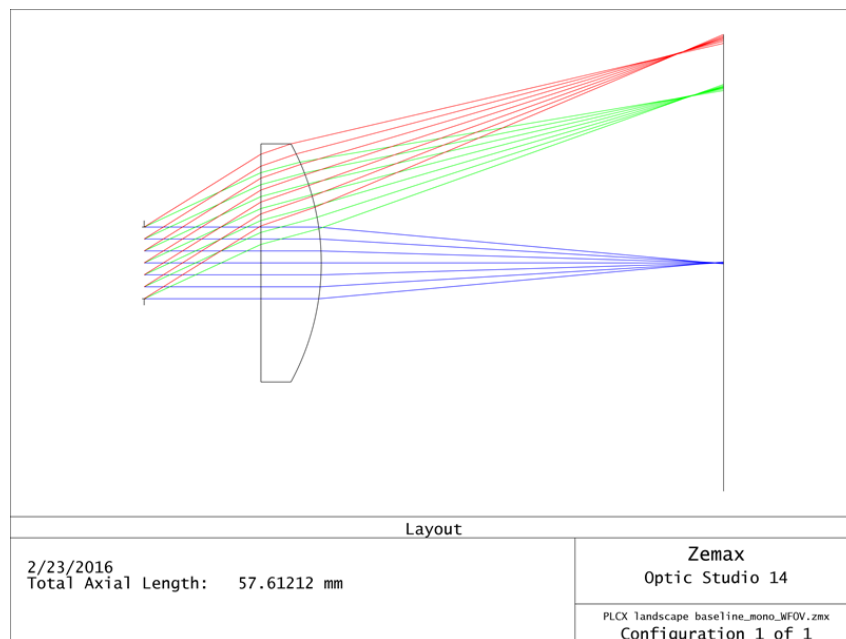


Figure 5 – Plano-convex landscape lens with optimally placed stop

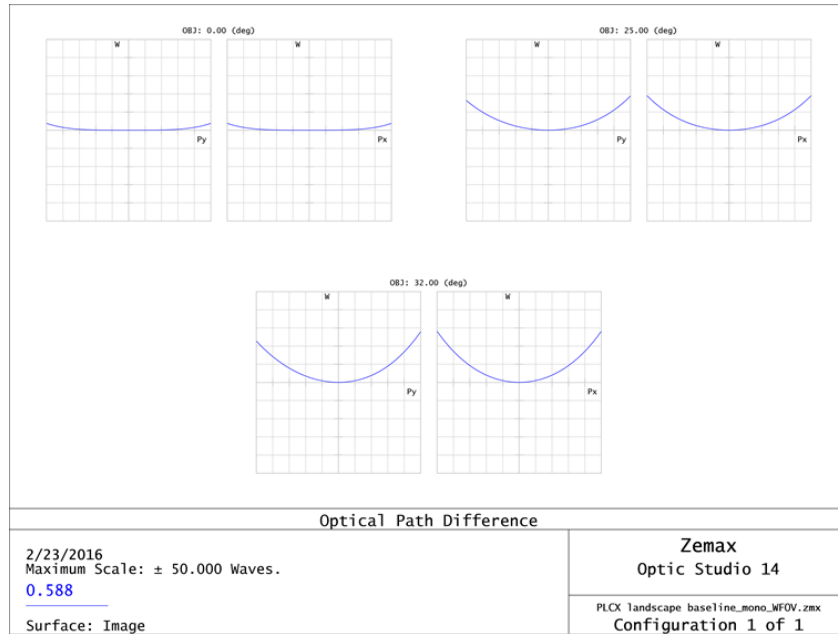


Figure 6 – OPD plots of plano-convex landscape lens with optimally placed stop

To build on this simple design approach, an even asphere lens is added at the aperture stop to correct SA. Since the goal with this design form is to achieve good correction on a curved focal surface, a multi-configuration model is developed which allows the focal distance to be independently optimized for each field angle, as shown in Figure 7.

Active : 2/3		Config 1	Config 2*	Config 3
1	THIC ▾ 4	32.525 V	30.651 V	29.543 V
2	YFIE ▾ 1	0.000	25.000	32.000

Figure 7 – Multi-configuration editor enabling evaluation on a curved image surface

Optimizing the second surface radii of both lenses along with the aspheric terms and stop position yields the design shown in Figure 8 and Figure 9. Freeing and optimizing the planar lens surface and the higher order aspheric terms were all found to have negligible effect on performance. The per-field angle performance depicted in Figure 10 demonstrates that excellent MTF over the field is achieved, except that the field is curved. Although the MTF curves indicate that diffraction-limited

performance is attained, we can see in the optical path difference (OPD) plots of Figure 11 that significant fourth order coma is being introduced to counter-balance higher order odd aberration.

	Surf.Type	Comment	Radius	Thickness	Material	Coating	Semi-Diameter	Conic	TCE x 1E-6	Par 1(unused)	Par 2(unused)	Pa
0	OBJECT	Standard ▾	Infinity	Infinity			0.000	0.000	0.000			
1		Standard ▾	Infinity	1.000	BK7		2.946	0.000	-			
2	STOP	Even Asphere ▾	-982.966 V	8.817 V			2.946	0.000	0.000	0.000	4.044E-005 V	
3		Standard ▾	Infinity	5.051	SK16		2.952	0.000	-			
4		Standard ▾	-20.704 V	32.747 V			2.953	0.000	0.000			
5	IMAGE	Standard ▾	Infinity	-			5.021E-003	0.000	0.000			

Figure 8 – Prescription for a monochromatic, plano-convex landscape lens with asphere at the stop

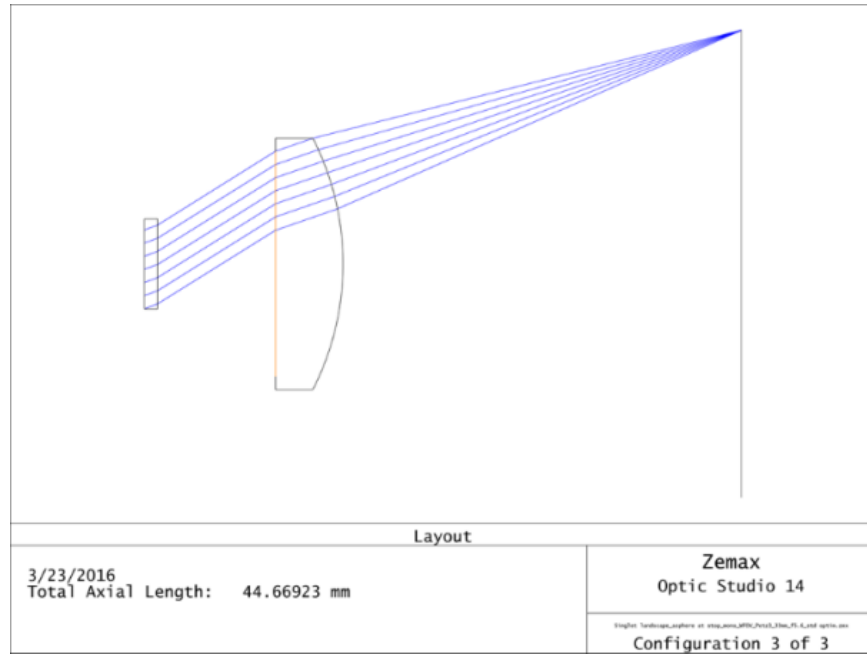


Figure 9 – Layout of plano-convex landscape lens with asphere at the stop

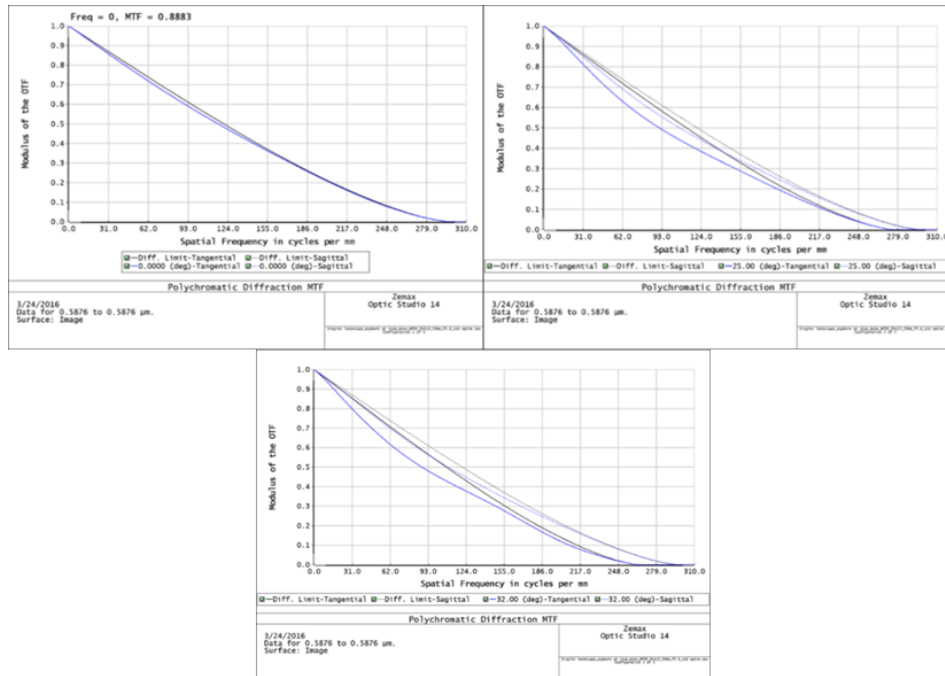


Figure 10 – MTF curves for three fields focused on a curved surface by the monochromatic, plano-convex landscape lens

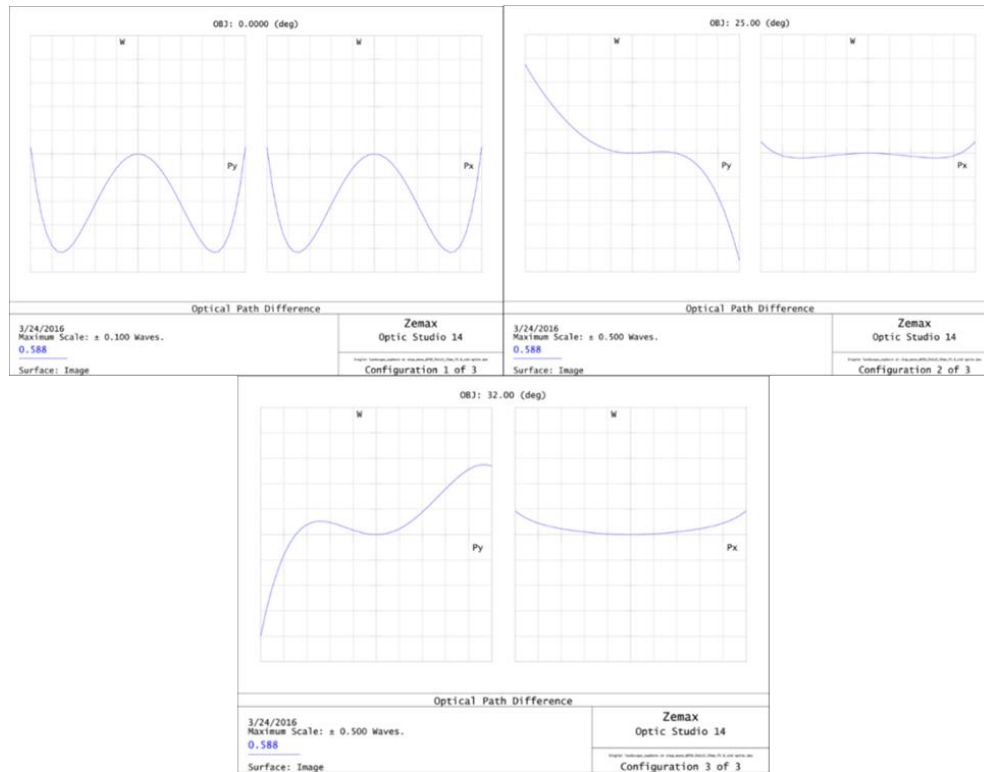


Figure 11 - Optical path difference plots for 3 fields focused on a curved surface by the monochromatic, plano-convex landscape lens

As attempts were made to extend this design form to be polychromatic, including converting both the aperture stop optic and the primary objective to achromatic or apochromatic doublets (Figure 12), the design form experienced degradation in the characteristics (identical correction of non-stigmatic aberrations over a curved field) which made it initially advantageous. Based on the sub-optimal performance attained on a curved image surface with four elements (Figure 13), and the apparent migration of the design form during optimization, the simple landscape lens was tabled in favor of an alternative design form known to be better suited to wide FOV operation.

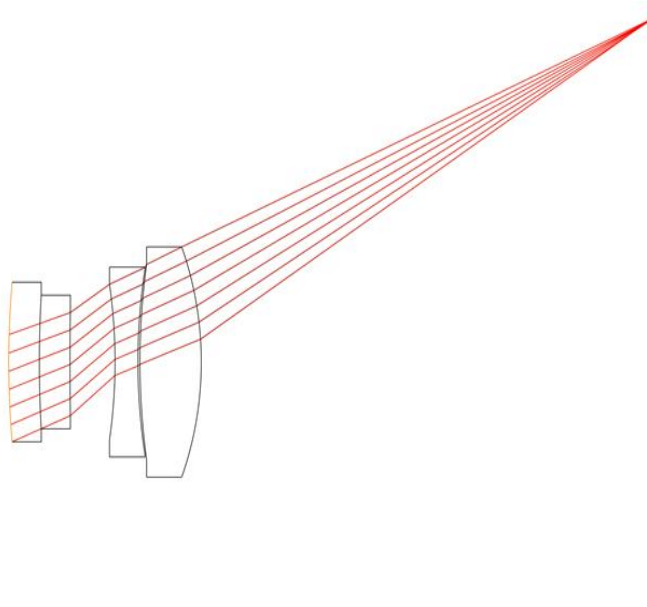


Figure 12 - Evolution of simple landscape lens for achromatization

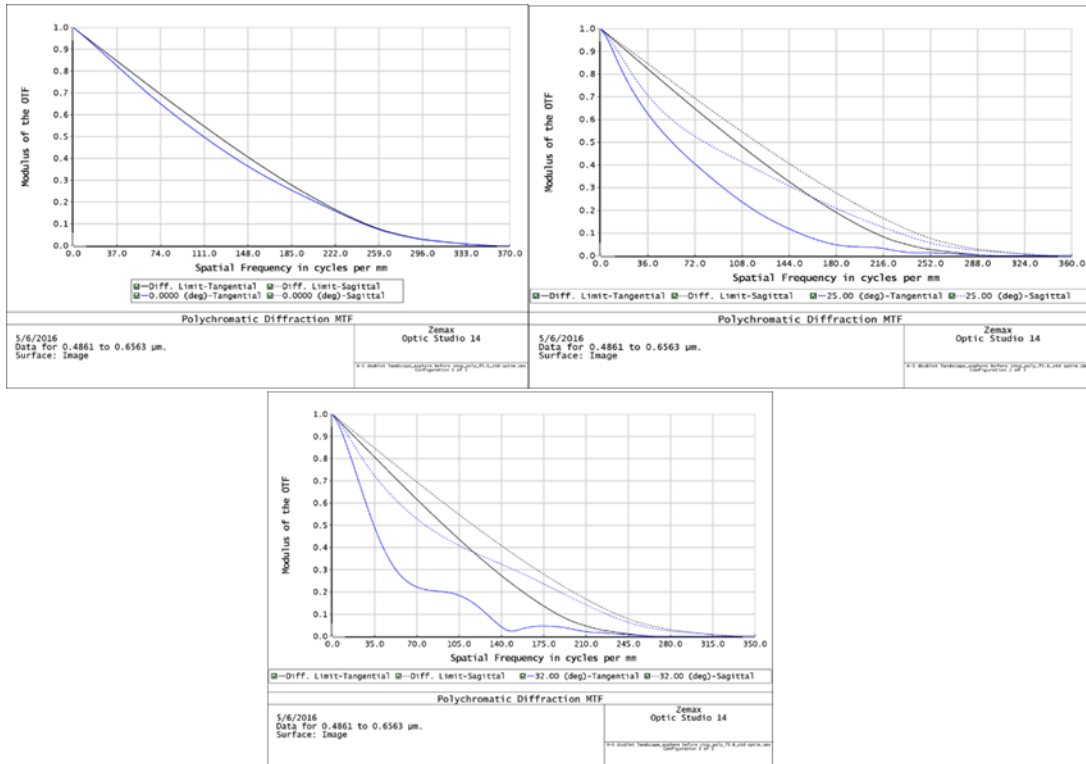


Figure 13 - MTF curves for polychromatic version of simple landscape lens

2.3.Simplification of a well-corrected WFOV lens: The Retrofocus Lens

The retrofocus lens is a reverse telephoto design form, which implies that it has an effective focal length which is shorter than the back focal distance. This is an ideal first order fit to our stated requirements since DSLR cameras require a 42mm back focal distance (BFD)¹ to give its mirror space to flip up and down. Retrofocus lenses can generally be thought of as being comprised by a front lens group, which is roughly afocal, and a rear focusing group, with the aperture stop located between them. The front afocal group is effectively like a beam expansion telescope, increasing the beam diameter while reducing the angle of incidence at the stop. From the object viewpoint, the telescope action appears as the inverse – reducing the beam size. This leads to a second advantage of the retrofocus architecture: a minified entrance pupil. The Lagrange invariant requires that the

¹ Rather than the back focal distance (BFD), typically it is an associated mechanical measurement called flange focal distance which is specified.

product of lens pupil diameter and chief ray angle is constant between the entrance and exit pupils [33], as described by equation (2):

$$H = n\bar{u}y_{pupil} = n'\bar{u}'y'_{pupil} , \quad (2)$$

where H is the Lagrange invariant, y_{pupil} and y'_{pupil} are the entrance and exit pupil heights respectively from the optical axis, and \bar{u} and \bar{u}' are the object space and image space chief rays respectively. For a system with the object and image in air this can be rewritten in terms of the pupil magnification as:

$$m_{pupil} = \frac{y'_{pupil}}{y_{pupil}} = \frac{\bar{u}}{\bar{u}'} \quad (3)$$

This relationship is shown in Figure 14 for a generic optical system which images an entrance pupil to an exit pupil with magnification >1 , thus requiring that the exit pupil chief ray is smaller than the entrance pupil chief ray.

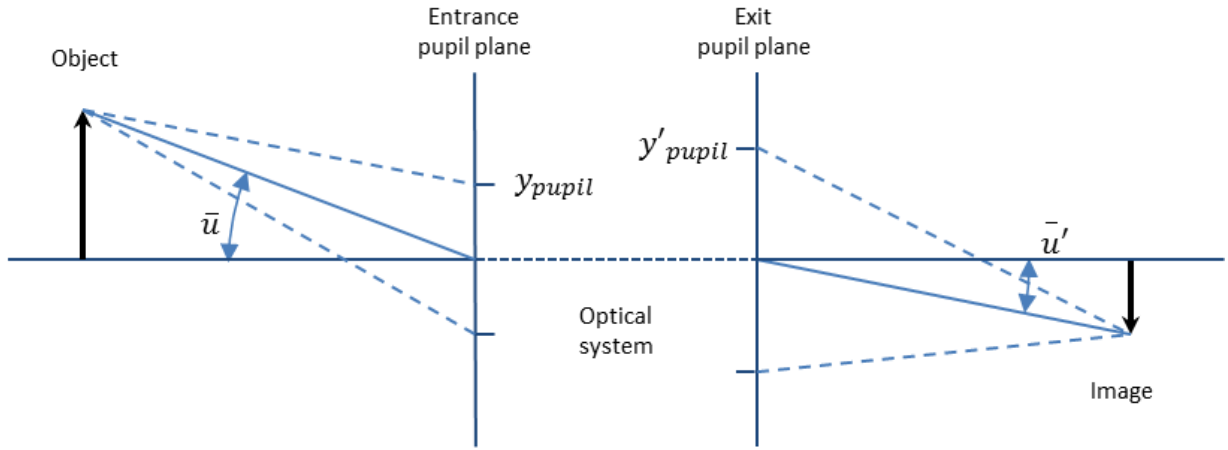


Figure 14 – Lagrange invariant relationship between entrance and exit pupil diameters and chief ray angles

Therefore, because our entrance chief ray angle and exit pupil diameter are fixed, the following linearly proportional relationship exists between the entrance pupil and exit chief ray:

$$\bar{u}' = y_{pupil} \left[\frac{2f/\#}{EFL} \cdot \bar{u} \right] = y_{pupil} \left[\frac{2 \cdot 5.6}{33mm} \cdot 32^\circ \right] \approx y_{pupil} \cdot 10.9^\circ/mm \quad (4)$$

This implies that the smaller we make the *entrance* pupil by design, the smaller the *image* space chief ray angle, which in turn reduces the obliquity experienced by the image space light cone at the edge

of the field. This is important for wide angle lenses for two reasons: reducing relative illumination fall-off with field angle and reducing numerical aperture (NA) fall-off with field angle. One of our principal goals for the new, field-invariant lens is MTF invariance with field angle, and the MTF cutoff frequency is inversely proportional to the working $f/\#$ [34] and thus is directly proportional to the NA. We would like to minimize the entrance pupil diameter and thus the image space field angle.

2.3.1. Lens design process and merit function design:

Existing retrofocus design examples were mined as starting points for both a baseline diffraction limited lens and for the field-invariant lens. Optimization of the baseline lens was more straightforward in that a standard default merit function using minimum root-mean-square (RMS) optical path difference (OPD) was suitable as the primary merit function content. For the field-invariant lens a more complex merit function was required, and as this lens was optimized, an optimum merit function was being developed in parallel. We describe this optimization in detail next. For both lens cases two key aspects of the merit function design included: (a) manual control of pupil aberrations to enable a physically realizable aperture stop, and (b) manually driving down the entrance pupil diameter in order to minimize NA fall-off at the edges of the field, as discussed above. For the pupil aberration, the principal solution was to add REAY² operands to the merit function for off-axis beam with a target intercept position of 0 at the stop location³. To drive down entrance pupil diameter, two different approaches were pursued: the first was to use entrance pupil and exit pupil diameter operands (EPDI⁴ and EXPD⁵) and a DIVI⁶ math operand to drive their ratio toward 0. The second approach, shown in

² REAY: OpticStudio merit function operand to control the real ray Y coordinate of a specific ray at a given optical surface.

³ It was later learned that a more efficient approach called “ray aiming” is available in OpticStudio for this purpose.

⁴ EPDI: OpticStudio merit function operand to control diameter of the entrance pupil.

⁵ EXPD: OpticStudio merit function operand to control diameter of the exit pupil.

⁶ DIVI: OpticStudio merit function operand to divide the values of any two other operands.

the merit functions in this section was to use TFNO⁷ operands for the tangential $f/\#$'s at the edge of the field and the on-axis field, and a DIVI math operand to drive their ratio toward 1. The two methods both worked reasonably, with their weightings needing to be adjusted multiple times to balance the full set of objectives.

2.3.2. Baseline design

To establish a baseline comparison lens design, we started with a published lens which is inherently well-corrected – although not quite diffraction-limited – over the full 64° FOV by design: an 8-element reverse telephoto (or “retrofocus”) lens that we adapt from a US patent by Mori [35][36]. This lens is at least as well-corrected, and least as simple, as several other retrofocus lens designs which evaluated as starting points – including a second patented lens by Mori and two sample lenses from the Zemax sample objectives included with OpticStudio™. The re-optimization of this lens began with scaling it to our focal length and establishing our fields and aperture. The combination of wide field angles, small entrance pupil, and large first element means that beam footprints at the first lens element were rather widely spaced with the standard 3-field approach. Thus to get a higher field sampling density five fields were used.

After adding the first order merit function constraints, and pupil aberration and obliquity control constraints discussed in section 2.3, an RMS OPD based default merit function was added. The final merit function is shown in Figure 15. Subsequent optimizations ultimately led to the removal of one of the three negative lens elements from the front group, the addition of even aspheres at three surfaces, and significant position shifting and curvature optimization. Multiple aspheric surfaces were evaluated, with the front surfaces of the first, third, and fifth elements ultimately settled on as providing the best performance achievable without adding a fourth asphere or breaking the cemented doublet. At the end the seven element (six physically

⁷ TFNO: OpticStudio merit function operand to control the lens $f/\#$ in the tangential direction.

separate) retrofocus lens described in Figure 16 and Figure 17 was developed, with three even aspheric surfaces. It should be noted that while substantial effort was put into lens optimization, and confidence is high that it is representative of a reasonable lower-limit of complexity, the design space exploration was not exhaustive.

	Type	Surf	Wave	Hx	Hy	Px	Py		Target	Weight	Value	% Contrib
1	EFFL		1						33.000	100.000	33.000	2.301E-00
2	MNCG	2	12						1.000	1.000	1.000	1.097E-00
3	MNEG	2	12	0.000					1.000	1.000	1.000	2.648E-00
4	MNCA	3	7						0.200	1.000	0.200	0.00
5	MNEA	3	7	0.000					0.200	1.000	0.200	3.138E-00
6	MNCA	8	9						0.000	1.000	0.000	0.00
7	MNEA	8	9	0.000					0.000	1.000	-4.738E-004	3.417E-00
8	MNCA	10	12						0.200	1.000	0.200	0.00
9	MNEA	10	12	0.000					0.200	1.000	0.199	0.00
10	MNCA	15	15						42.000	1.000	42.000	2.244E-00
11	MXCG	2	12						8.000	1.000	8.000	0.00
12	TFNO	1	1						0.000	0.000	5.606	0.00
13	TFNO	3	1						0.000	0.000	5.981	0.00
14	DIVI	12	13						1.000	0.000	0.937	0.00
15	TFNO	4	1						0.000	0.000	6.050	0.00
16	DIVI	12	15						1.000	0.500	0.927	13.23
17	TFNO	5	1						0.000	0.000	6.003	0.00
18	DIVI	12	17						1.000	0.500	0.934	6.12
19	REAY	9	2	0.000	0.700	0.000	0.000		0.000	0.200	0.071	9.25
20	REAY	9	2	0.000	1.000	0.000	0.000		0.000	0.200	-0.048	4.03
21	TOTR								0.000	0.000	122.000	0.00
22	OPLT	21							122.000	1.000	122.000	4.094E-00
23	DMFS											
24	BLNK	Sequential merit function: RMS wavefront centroid GQ 8 rings 8 arms										

Figure 15 – Optimization merit function for the baseline retrofocus lens

Surf	Type	Comment	Radius	Thickness	Material	Coating	Semi-Diameter	Conic	TCE x 1E-6	2nd Order Ter	4th Order Ter	6th Order Ter	8th Order Ter
0	OBJECT	Standard	Infinity	Infinity			Infinity	0.000	0.000				
1		Standard	Infinity	2.000			19.667	0.000	0.000				
2		Even Asphere	42.227 V	2.000	LAKN7		16.204	0.000	-	0.000	5.071E-006 V	-1.220E-010 V	-8.190E-012 V
3		Standard	18.518 V	7.860 V			13.668	0.000	0.000				
4		Standard	-57.392 V	1.800	LAKN7		13.608	0.000	-				
5		Standard	42.524 V	12.137 V			13.221	0.000	0.000				
6		Even Asphere	29.601 V	3.000	BAF10		14.569	0.000	-	0.000	-1.106E-005 V	-1.928E-009 V	0.000
7		Standard	44.577 V	5.000	LACL4		14.343	0.000	-				
8		Standard	-62.969 V	23.842 V			14.234	0.000	0.000				
9	STOP	Standard	Infinity	0.187 V			4.733	0.000	0.000				
10		Even Asphere	-60.771 V	1.000 V	SF4		4.733	0.000	-	0.000	-7.128E-006 V	2.073E-007 V	-5.190E-009 V
11		Standard	32.910 V	0.230 V			4.761	0.000	0.000				
12		Standard	36.573 V	1.959	SK2		4.789	0.000	-				
13		Standard	-26.161 V	16.782 V			4.925	0.000	0.000				
14		Standard	33.778 V	2.204	LAKN6		10.779	0.000	-				
15		Standard	64.207 V	42.000 M			10.836	0.000	0.000				
16	IMAGE	Standard	Infinity	-			18.392	0.000	0.000				

Figure 16 – Lens prescription for the baseline retrofocus lens

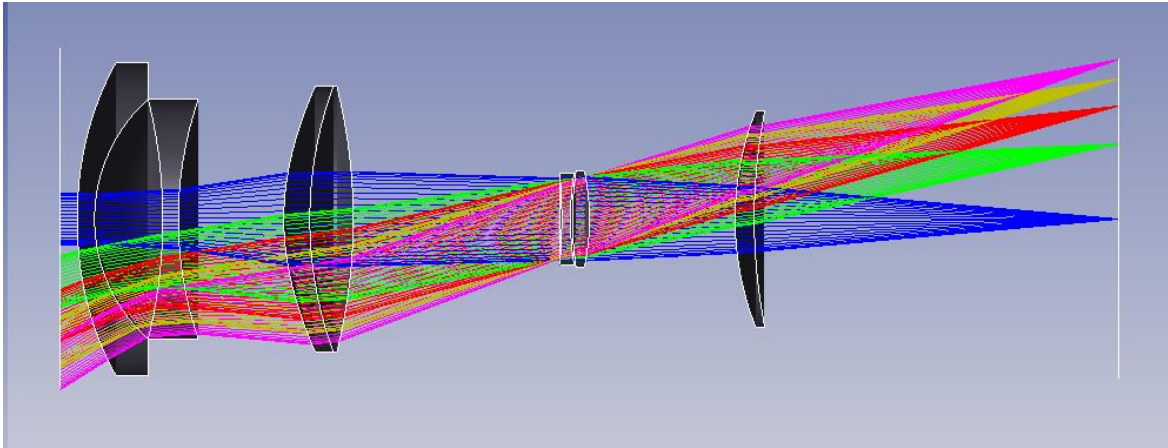


Figure 17 – Ray-trace diagram for the baseline retrofocus lens

As is evident from the MTF plots of Figure 18, in which the solid black line represents the on-axis diffraction limit, decent performance is achieved at all field angles. It can also be seen that the maximum field cutoff frequency is not shifted downward from the on-axis cutoff frequency. While it is not immediately obvious from this family of MTF curves, nor from the geometric spot diagrams of Figure 19, whether diffraction limit is actually attained, study of the RMS wavefront error vs. field in Figure 20 and the Strehl ratio (SR)⁸ vs. field in Figure 21 reveal that the polychromatic RMS wavefront error is below the diffraction limit (the straight line) and that the average SR is consistently above 0.8, which is also an indicator of the diffraction limit. Performance data for the OPD vs. field, field curvature and distortion, and relative distortion are depicted in Figure 22, Figure 23, and Figure 24 respectively. Figure 25 shows a composite of the diffraction PSFs at all five modeled fields, and their consistent airy shape is another indicator that aberrations are in check. For completeness Figure 26 shows a composite of the exit pupil phase maps over the field.

⁸ The Strehl ratio (SR), a single number indicator of the image quality, is defined as the ratio of the peak value of the real PSF divided by the peak value of the diffraction-limited PSF.

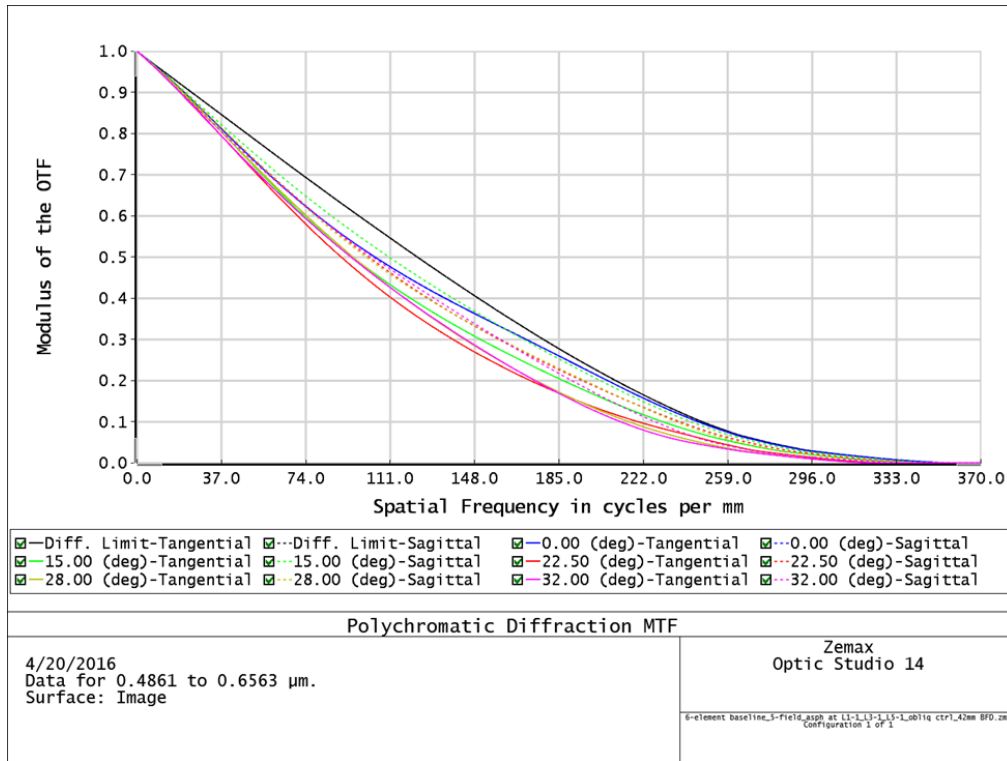


Figure 18 – Family of MTF curves for all fields of the baseline retrofocus lens, including the on-axis diffraction limit



Figure 19 – Matrix of geometric spot diagrams for the baseline retrofocus lens across wavelengths for all fields.

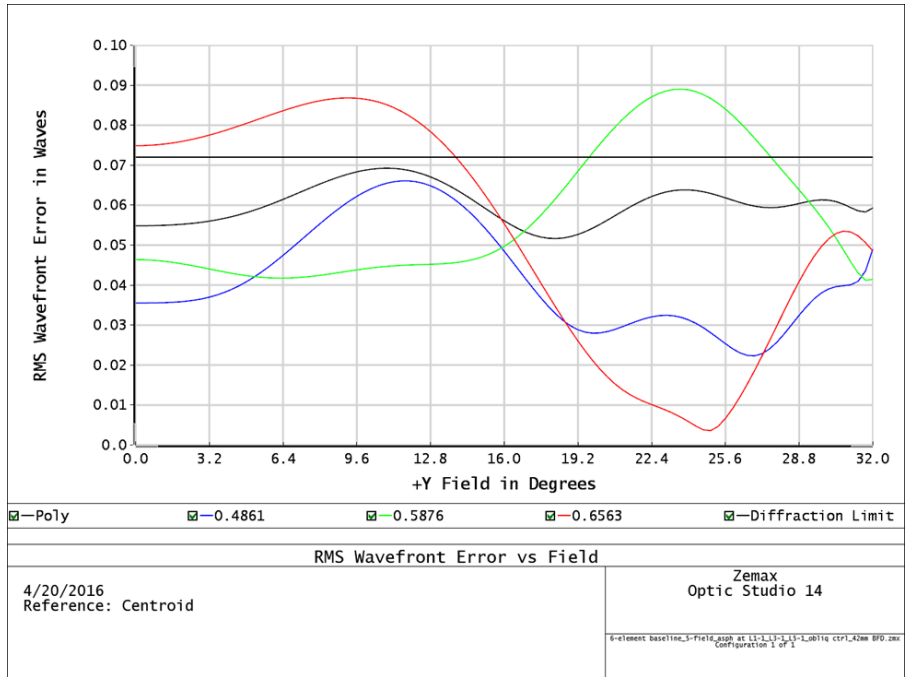


Figure 20 – Plots of RMS wavefront error of the baseline retrofocus lens vs. field for each wavelength plus the polychromatic average. The diffraction limit is shown as a reference.

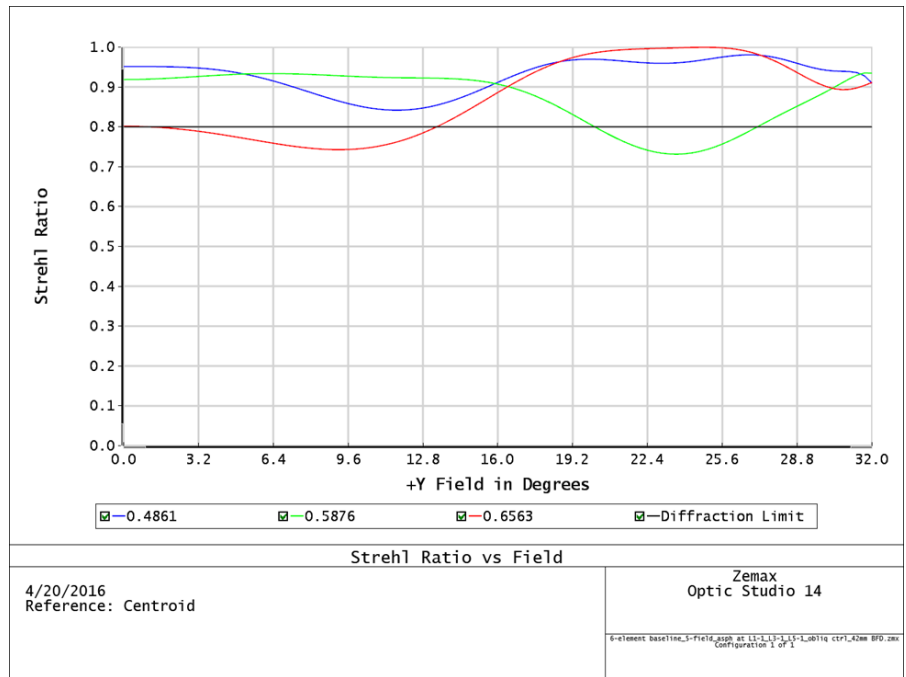


Figure 21 – Plots of Strehl ratio vs. field for each wavelength for the baseline retrofocus lens. The diffraction limit value of 0.8 is shown as a reference.

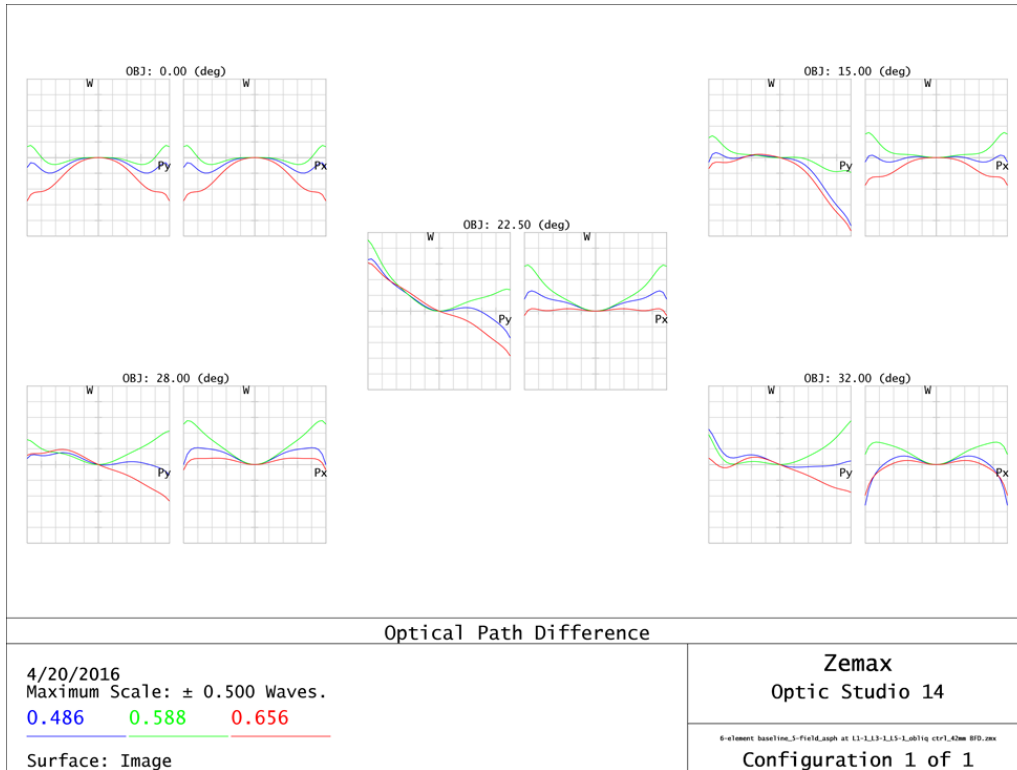


Figure 22 – Family of OPD plots for each wavelength and field position for the baseline retrofocus lens.

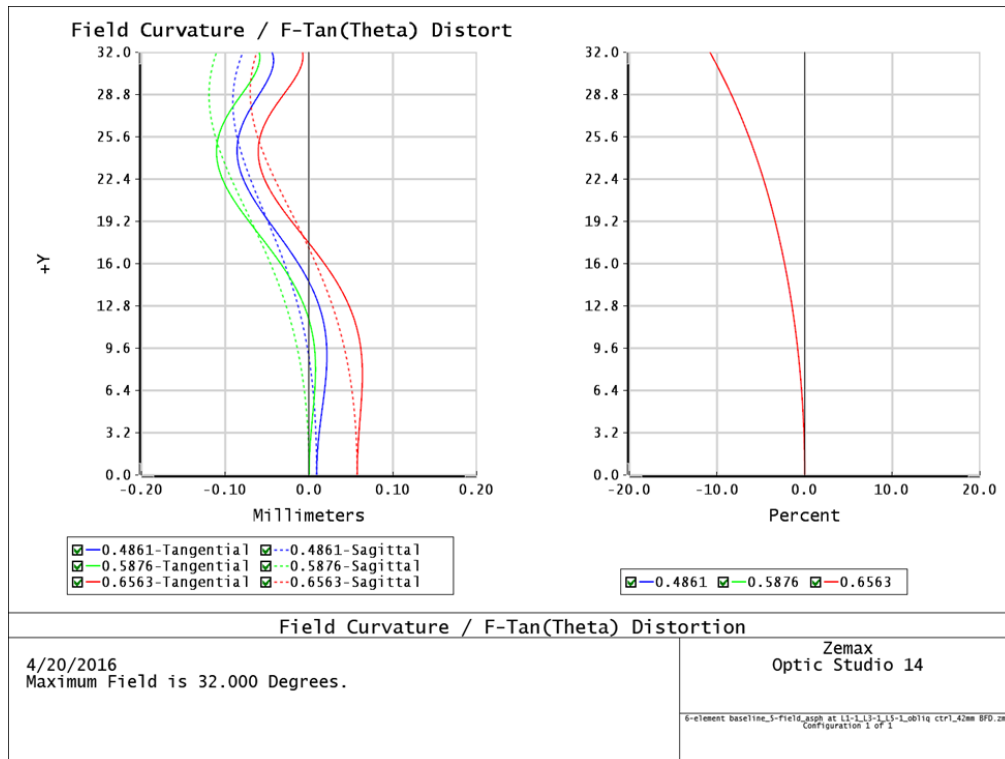


Figure 23 – Field curvature and distortion plots for the baseline retrofocus lens.

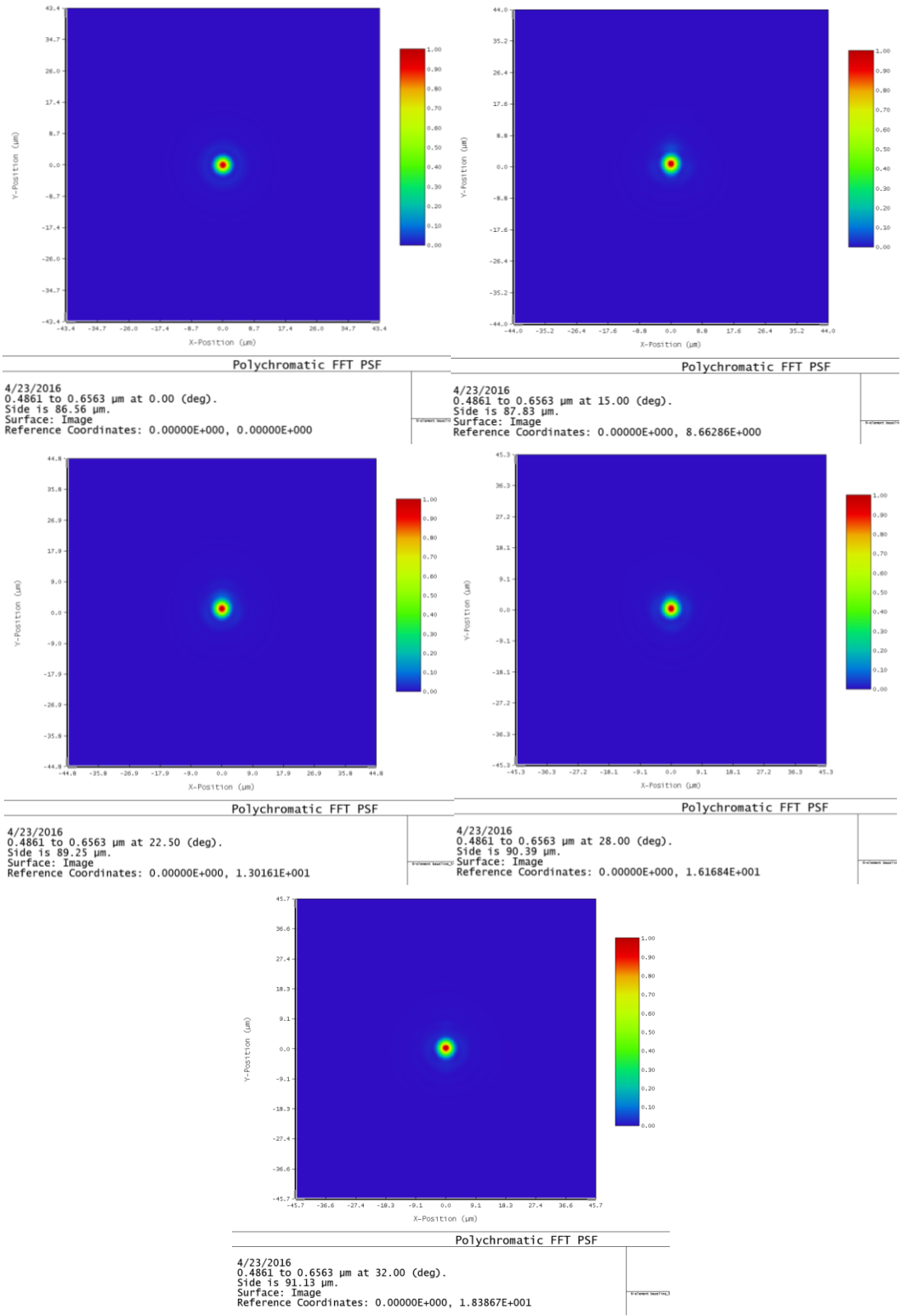


Figure 25 – Composite of diffraction PSFs for the baseline retrofocus lens for all five field angles.

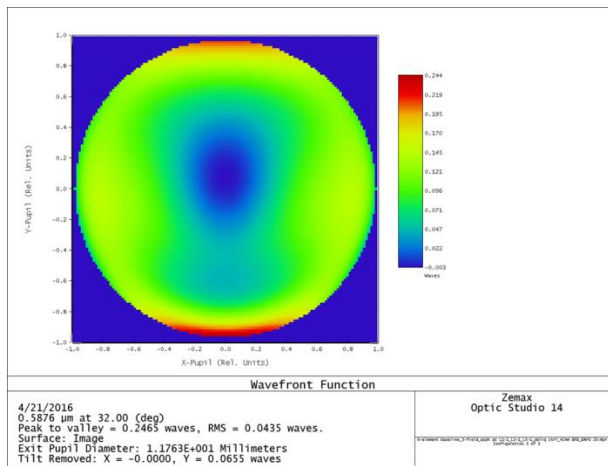
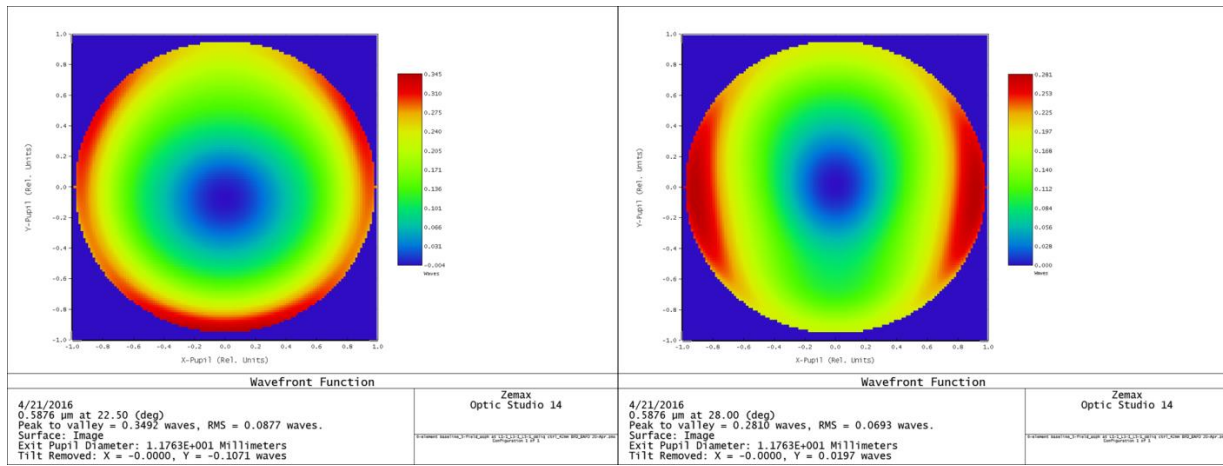
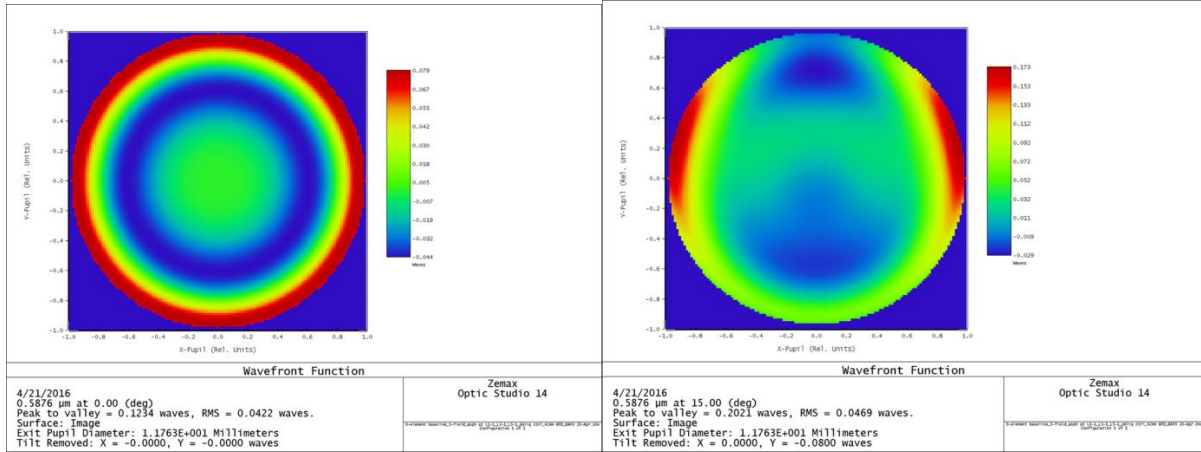


Figure 26 - Composite of exit pupil wavefront surface maps for the baseline retrofocus lens for all five field angles.

2.3.3. Design of the field-invariant retrofocus lens

The objective here was to find a lens satisfying the same first order requirements as the baseline lens, but with the diffraction limit requirement relaxed. In its place is a requirement that the MTF curves be well matched over all field angles and the full spatial frequency domain. A US Patent by Momiyama [33][36] was identified as an attractive starting point for a field-invariant design. This is a 6-element, f/2.8 polychromatic lens as designed, and after scaling it to 33mm focal length and down-sizing the aperture to f/5.6, it yielded the lens as depicted in Figure 27.

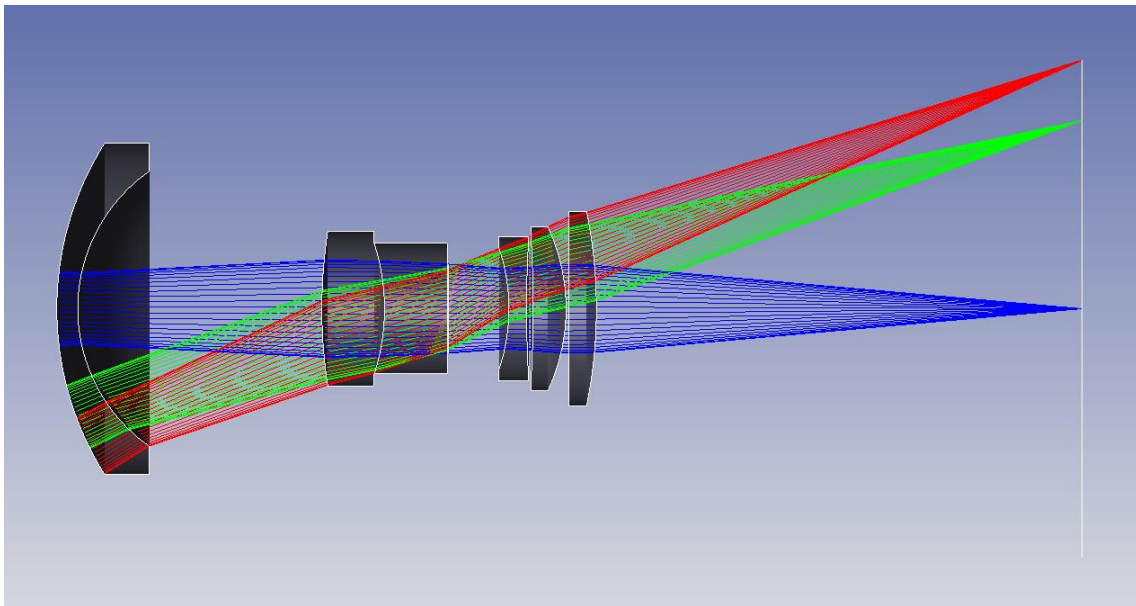


Figure 27 – Starting point for design of the field-invariant lens.

A merit function was developed which encompassed all of the features discussed in the baseline lens section. Additionally, this merit function is modified to enforce MTF consistency over the field and across spatial frequencies while maintaining reasonable overall MTF. The final goal which needed to be kept in mind is that we planned from the start to deconvolve the resulting PSF with a Wiener filter, which will amplify image noise to a degree proportional to the area between our MTF curve and a diffraction-limited MTF curve. Ultimately lens optimization needed to be executed in two phases: first a basic optimization using primarily an rms OPD minimization, and second a relative MTF based merit function.

These two phases had to be repeated any time a manual change to the model caused the performance to deteriorate to an unacceptable level. This occurred because the relative MTF merit function, depicted in Figure 28, was not useful for finding solutions that were not already close to optimum. To achieve the MTF matching, a full family of tangential and sagittal MTF operands was added to cover all five field angles and two different spatial frequencies. Frequencies of 100mm^{-1} and 220mm^{-1} were empirically deemed to be optimum. MINN⁹, MAXX¹⁰, DIFF¹¹, and ABSO¹² operands were then added to produce a single operand whose value represented the range of MTF values at that frequency. This gave us two operands to drive toward zero. Lastly, for each of the two frequencies, OPGT¹³ operands were added which were aimed at the MINN operand to ensure the minimum MTF value across field angles would drive to be greater than some manually determined value. These kept the MTF as high as reasonably possible while still enforcing equivalence over the field.

⁹ MINN: OpticStudio merit function operand to find the minimum value among a range of other operands.

¹⁰ MAXX: OpticStudio merit function operand to find the maximum value among a range of other operands.

¹¹ DIFF: OpticStudio merit function operand to subtract the values of two other operands.

¹² ABSO: OpticStudio merit function operand to calculate the absolute value of another operand.

¹³ OPGT: OpticStudio merit function operand to constrain the value of another operand to be greater than a target value.

	Type	Op#				Target	Weight	Value	% Contrib	
1	EFFL	1				33.000	100.000	32.997	0.000	
2	MXCG	2	12			12.000	1.000	12.000	0.000	
3	MNEG	2	12	0.000		0.500	1.000	0.476	0.000	
4	MNCA	2	4			0.200	1.000	0.200	0.000	
5	MNEA	2	4	0.000		0.200	1.000	0.200	0.000	
6	MNCA	5	6			0.000	1.000	0.000	0.000	
7	MNEA	5	6	0.000		0.000	1.000	-3.718E-003	0.000	
8	MNCA	9	10			0.200	1.000	0.200	0.000	
9	MNEA	9	10	0.000		0.200	1.000	0.200	0.000	
10	TOTR					0.000	0.000	103.059	0.000	
11	OPLT	10				122.000	1.000	122.000	0.000	
12	TFNO	1	1			0.000	0.000	5.593	0.000	
13	TFNO	3	1			0.000	0.000	5.999	0.000	
14	DIVI	12	13			1.000	0.000	0.932	0.000	
15	TFNO	4	1			0.000	0.000	6.157	0.000	
16	DIVI	12	15			1.000	0.000	0.908	0.000	
17	TFNO	5	1			0.000	0.000	6.239	0.000	
18	DIVI	12	17			1.000	2.000	0.896	0.000	
19	REAY	6	2	0.000	0.700	0.000	0.000	0.018	0.000	
20	REAY	6	2	0.000	1.000	0.000	0.000	-0.028	0.000	
21	TOTR					0.000	0.000	103.059	0.000	
22	OPLT	21				122.000	1.000	122.000	0.000	
23	MTFS	3	0	1	100.0	1	0.000	0.000	0.151	0.000
24	MTFT	3	0	1	100.0	1	0.000	0.000	0.125	0.000
25	MTFS	3	0	2	100.0	1	0.000	0.000	0.205	0.000
26	MTFT	3	0	2	100.0	1	0.000	0.000	0.169	0.000
27	MTFS	3	0	3	100.0	1	0.000	0.000	0.147	0.000
28	MTFT	3	0	3	100.0	1	0.000	0.000	0.182	0.000
29	MTFS	3	0	4	100.0	1	0.000	0.000	0.168	0.000
30	MTFT	3	0	4	100.0	1	0.000	0.000	0.143	0.000
31	MTFS	3	0	5	100.0	1	0.000	0.000	0.234	0.000
32	MTFT	3	0	5	100.0	1	0.000	0.000	0.142	0.000
33	MINN	23	32			0.000	0.000	0.125	0.000	
34	MAXX	23	32			0.000	0.000	0.234	0.000	
35	DIFF	33	34			0.000	0.000	-0.110	0.000	
36	ABSO	35				0.000	10.000	0.110	0.000	
37	OPGT	33				0.125	100.000	0.125	0.000	
38	MTFS	3	0	1	220.0	1	0.000	0.000	0.054	0.000
39	MTFT	3	0	1	220.0	1	0.000	0.000	0.065	0.000
40	MTFS	3	0	2	220.0	1	0.000	0.000	0.063	0.000
41	MTFT	3	0	2	220.0	1	0.000	0.000	0.077	0.000
42	MTFS	3	0	3	220.0	1	0.000	0.000	0.052	0.000
43	MTFT	3	0	3	220.0	1	0.000	0.000	0.049	0.000
44	MTFS	3	0	4	220.0	1	0.000	0.000	0.057	0.000
45	MTFT	3	0	4	220.0	1	0.000	0.000	0.030	0.000
46	MTFS	3	0	5	220.0	1	0.000	0.000	0.030	0.000
47	MTFT	3	0	5	220.0	1	0.000	0.000	0.030	0.000
48	MINN	38	47			0.000	0.000	0.030	0.000	
49	MAXX	38	47			0.000	0.000	0.077	0.000	
50	DIFF	48	49			0.000	0.000	-0.048	0.000	
51	ABSO	50				0.000	50.000	0.048	0.000	
52	OPGT	48				0.060	200.000	0.030	0.000	

Figure 28 – Complete OpticStudio merit function for field-invariant retrofocus lens.

To adapt this lens for our purposes we replaced the cemented doublet element with a singlet and then re-optimized initially for single wavelength, towards diffraction-limited performance. Subsequent to re-adding the red and blue wavelengths, substantial effort was expended to achieve polychromatic performance which met our field-invariance criteria without adding more elements. Multiple even aspheres were allowed as in the baseline lens, and numerous glass combinations and asphere locations were pursued. Ultimately the best performance that could be attained with these constraints was with the configuration shown in Figure 29 and Figure 30, with resulting MTF curves as shown in Figure 31. While the MTF field-invariance appears good over much of the frequency band, at the higher end (above 220 mm⁻¹), there was insufficient leverage in the available degrees of freedom to drive the off-axis MTF levels away from zero. This was deemed to be inadequate for our purposes, as the Wiener filter would

lead to higher gain in that band to elevate the system MTF level adequately, although at the cost of significant noise gain.

Surf.	Surf.Type	Comment	Radius	Thickness	Material	Coating	Semi-Diameter	Conic	TCE x 1E-6	2nd Order Term	4th Order Term	6th Order Term	8th Order Term	10th Order Term
0	OBJECT	Standard	Infinity	Infinity			Infinity	0.000	0.000					
1		Standard	Infinity	2.000			20.805	0.000	0.000					
2	Even Asphere		129.778 V	3.000	N-SK16		18.503	0.000	-	0.000	2.830E-006 V	6.520E-010 V	0.000	
3		Standard	19.906 V	49.878 V			14.877	0.000	0.000					
4		Standard	15.984 V	4.000	P-LAF37		9.245	0.000	-					
5		Standard	15.900 V	6.000	N-SK16		8.121	0.000	-					
6	Even Asphere		47.922 V	4.324 V			6.772	0.000	0.000	0.000	-2.627E-005 V	-1.096E-007 V	5.459E-010 V	
7	STOP		Infinity	0.000			5.113	0.000	0.000					
8		Standard	14.665 V	3.000	FK54		4.857	0.000	-					
9		Standard	-12.360 V	1.500	BASF52		4.598	0.000	-					
10	Even Asphere		36.292 V	47.842 M			4.562	0.000	0.000	0.000	9.860E-005 V	-3.973E-007 V	1.177E-008 V	
11	IMAGE		Infinity	-			19.818	0.000	0.000					

Figure 29 – Lens prescription for initial design of field-invariant retrofocus lens.

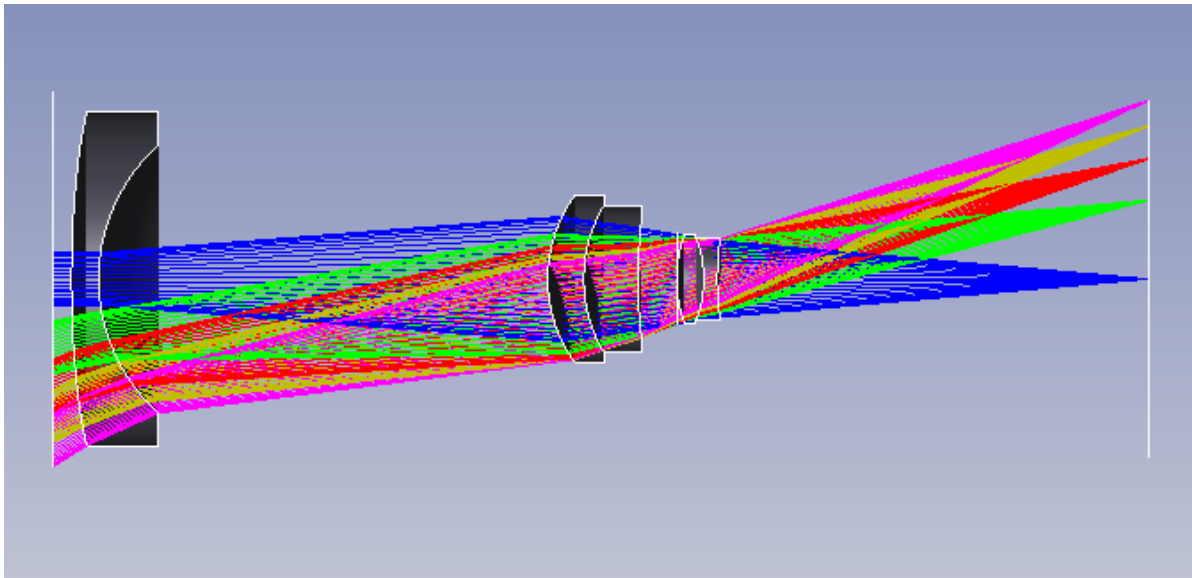


Figure 30 - Ray-trace diagram for initial design of field-invariant retrofocus lens.

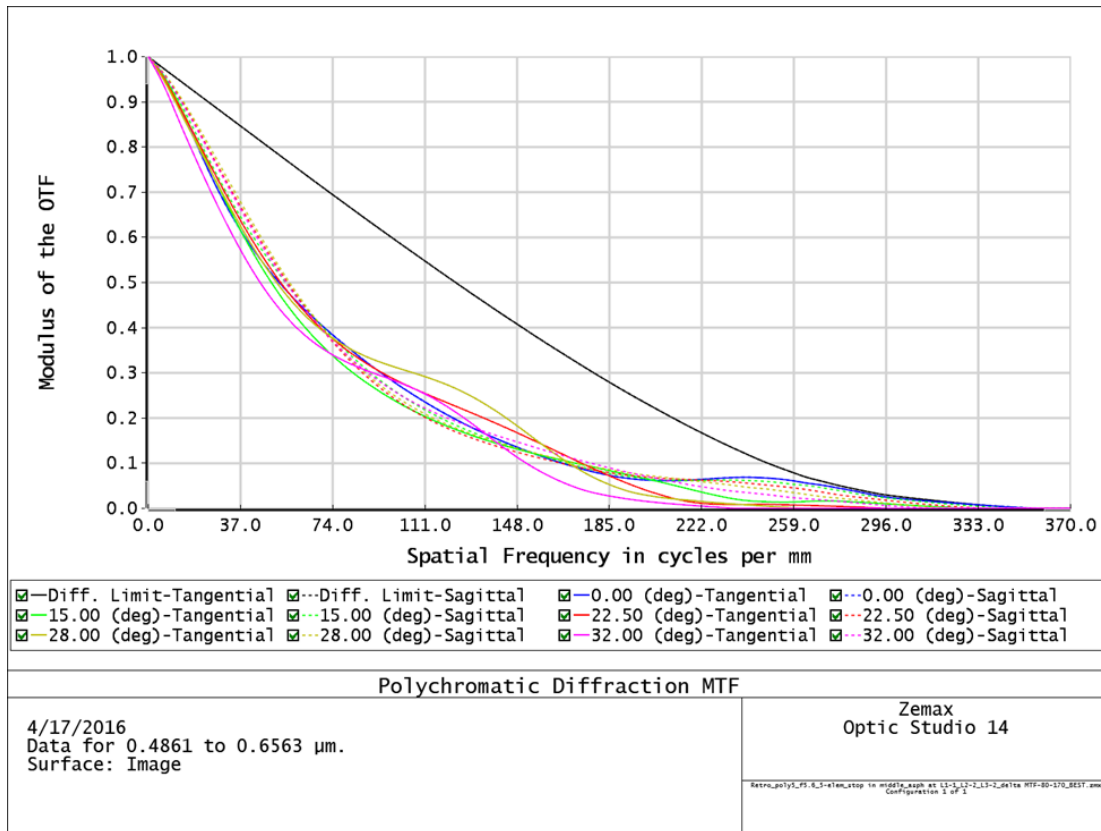


Figure 31 – Family of MTF curves for initial design of field-invariant retrofocus lens, plus diffraction limit.

To enable reasonable MTF levels at high spatial frequencies, it was decided that an asymmetric aspheric must be explored. As had been done with traditional EDoF wavefront coding masks, it was decided to try the asymmetric surface at the aperture stop where it could be combined with one of the even aspheric optical surfaces. In theory, this would help ease the burden borne by the other optics for defocus, FC, and axial chromatic aberrations as claimed in the literature. A Zernike sag surface was employed, which includes provisions for standard even polynomial terms as well as Zernike polynomial terms as defined in [39]. As a minimum, we assumed cubic terms (Z_7 and Z_8) would be necessary, but due to improvements claimed by inclusion of higher order terms ([9][10][11][12]), it was decided to also free the trefoil radial third order terms (Z_9 and Z_{10}) and the radial fifth order terms (Z_{16} through Z_{21}). Subsequent optimizations led to a five element retrofocus lens (three physically separate), with three aspheric surfaces which ultimately appeared to meet our requirements. Two of the aspherics are even

order polynomials as in the baseline design, and one aspheric is a combination of an even polynomial plus the 3rd and 5th order odd (asymmetric) Zernike terms. The lens is detailed in Figure 32 and Figure 33, with the family of MTF curves shown in Figure 34. While MTF at the highest frequencies is not as high as we might like, there is non-negligible modulation in the lowest curves out to a spatial frequency of about 300mm^{-1} , which is $0.8 \times f_{cutoff}$ for the blue. This lens is our candidate for Wiener deconvolution to restore a full system transfer function (STF) which approximates diffraction limit.

	SurfType	Radius	Thickness	Material	Semi-Diameter	4th Order Term	6th Order Term	8th Order Term	Zernike 7	Zernike 8	Zernike 9	Zernike 10	Zernike 16	Zernike 17	Zernike 18	Zernike 19	Zernike 20	Zernike 21
0	OBJECT	Standard	Infinity	Infinity	Infinity													
1	Standard	Infinity	2.000		22.000													
2	(aper) Even Asphere	75.286	3.000	N-PSK58	18.000	4.121E-006	-4.162E-009	-4.032E-013										
3	(aper) Standard	18.534	26.058		14.500													
4	(aper) Even Asphere	12.791	4.841	P-LAF37	8.800	-1.348E-005	-4.265E-008	6.615E-011										
5	(aper) Standard	14.473	7.827		6.800													
6	STOP	Standard	Infinity	0.559	4.147													
7	(aper) Zernike Standard Sag	-15.790	4.916	N-SK16	4.500	-2.500E-005	1.057E-007	-2.075E-008	-5.072E-005 V	7.408E-005 V	-6.159E-005 V	-1.237E-005 V	-3.047E-006 V	2.443E-005 V	-1.177E-001 V	-7.124E-006 V	4.151E-007 V	-5.633E-006 V
8	(aper) Standard	-15.757	0.200		6.000													
9	(aper) Standard	25.305	3.000	FK4	6.400													
10	(aper) Standard	-11.315	0.200		6.400													
11	(aper) Standard	-11.683	1.500	BASF32	6.400													
12	(aper) Standard	-35.669	48.958 M		7.000													
13	IMAGE	Standard	Infinity	-	18.613													

Figure 32 – Lens prescription for field-invariant retrofocus lens.

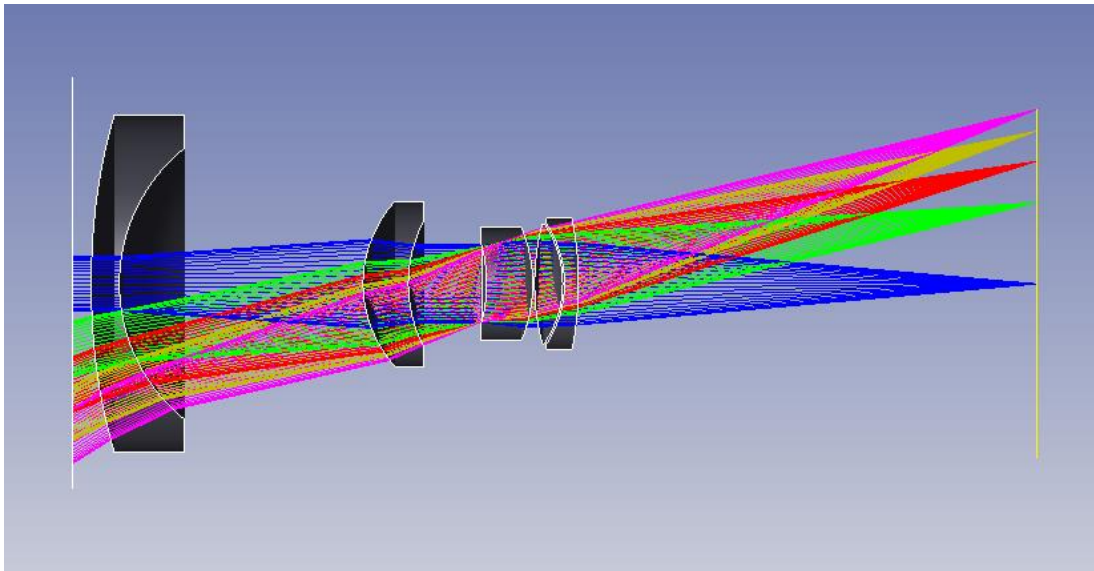


Figure 33 – Ray-trace diagram for field-invariant retrofocus lens.

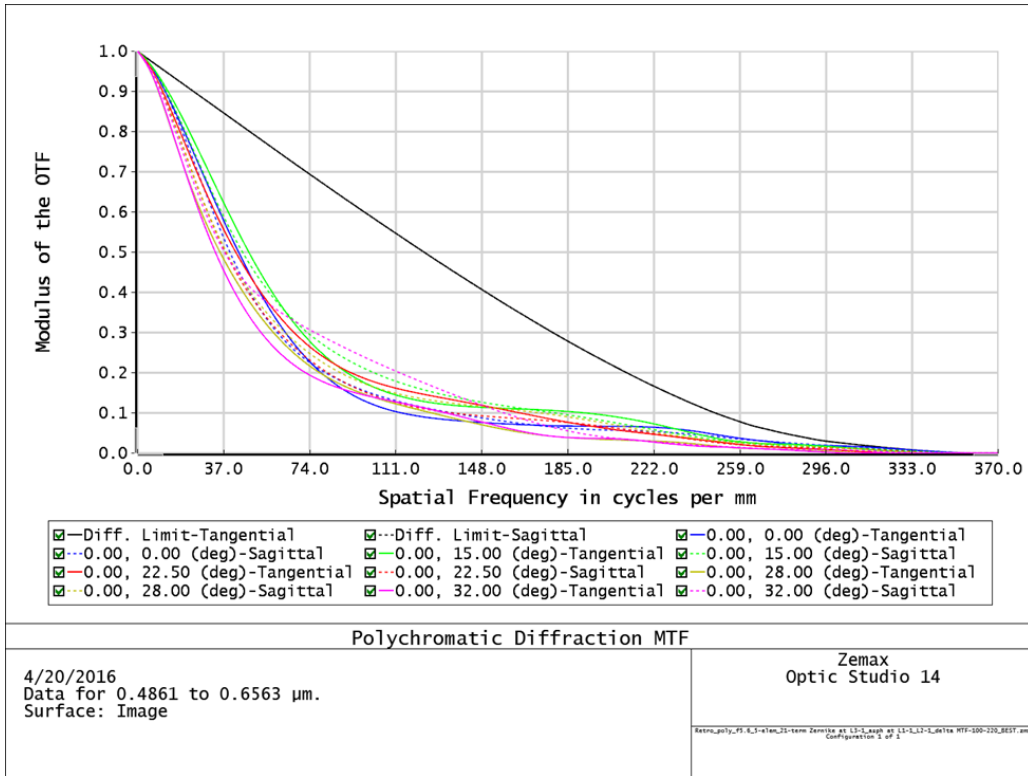


Figure 34 – Family of MTF curves for field-invariant retrofocus lens, plus diffraction limit.

The degree of field invariance is further illustrated in the following plots of MTF vs. field (Figure 35), geometric spot sizes vs. field (Figure 36), RMS wavefront error vs. field (Figure 37), and Strehl ratio vs. field (Figure 38). It is also noted that the rms wavefront error and Strehl ratio are now both distinctly on the aberrated side of diffraction limit.

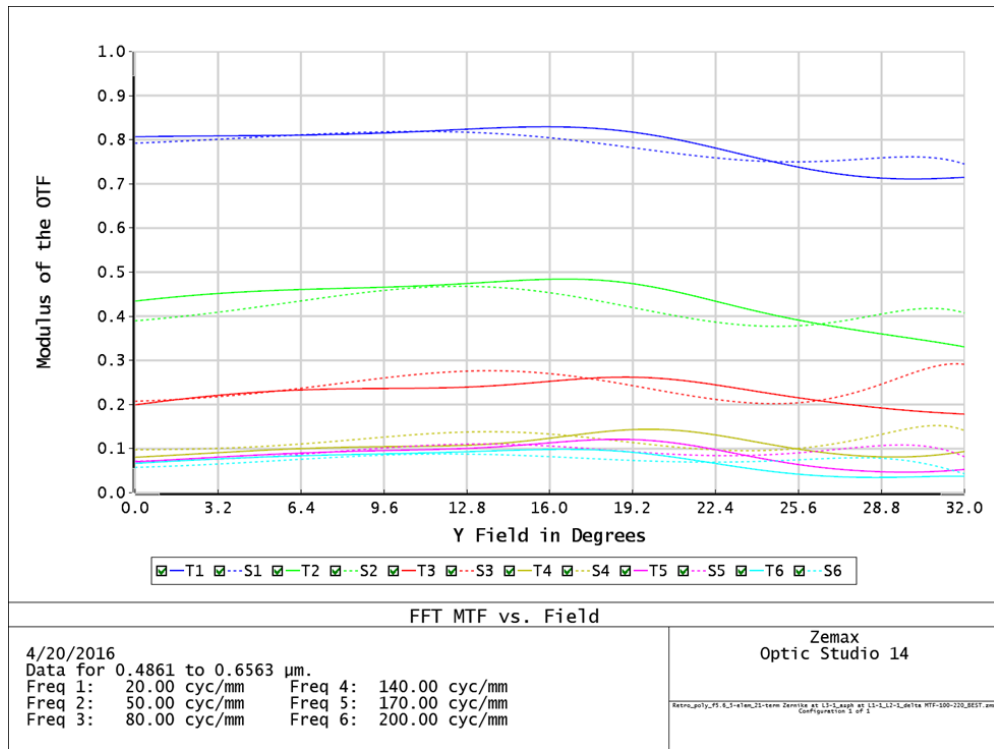


Figure 35 – Plots of MTF vs. field at five different spatial frequencies for field-invariant retrofocus lens.

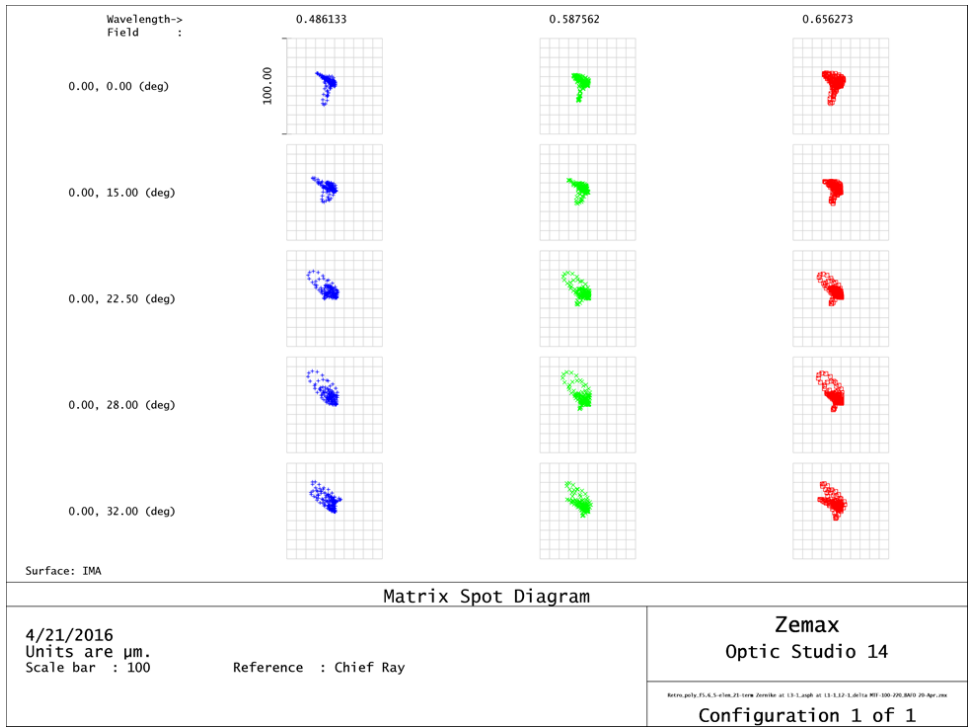


Figure 36 – Matrix of geometric spot diagrams across wavelengths for all fields for field-invariant retrofocus lens.

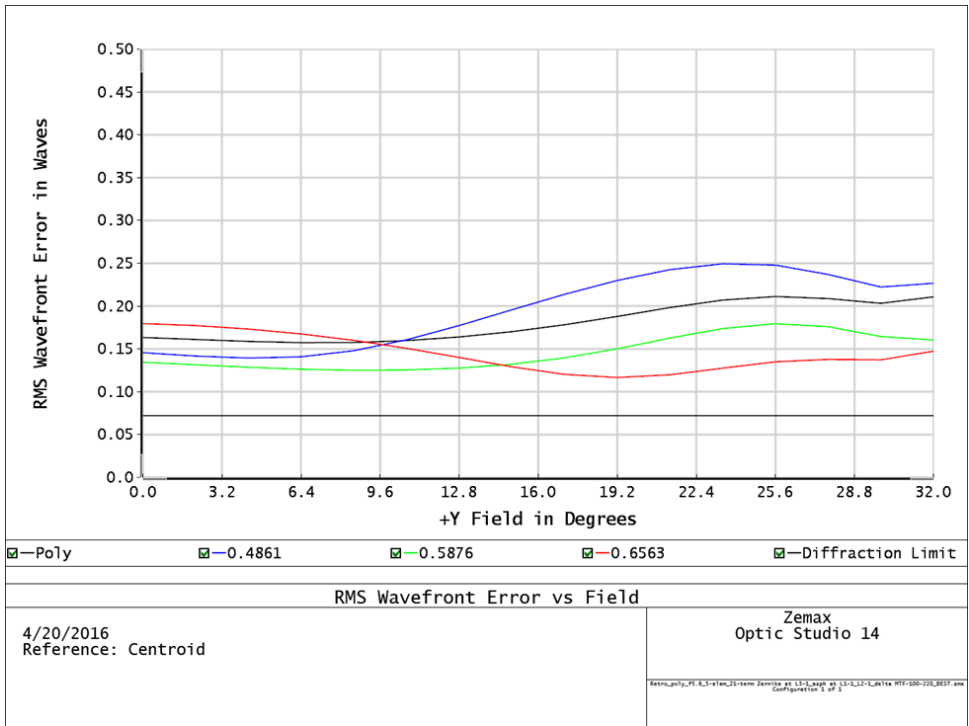


Figure 37 – Plots of RMS wavefront error for field-invariant retrofocus lens vs. field for all wavelengths and for the polychromatic average.

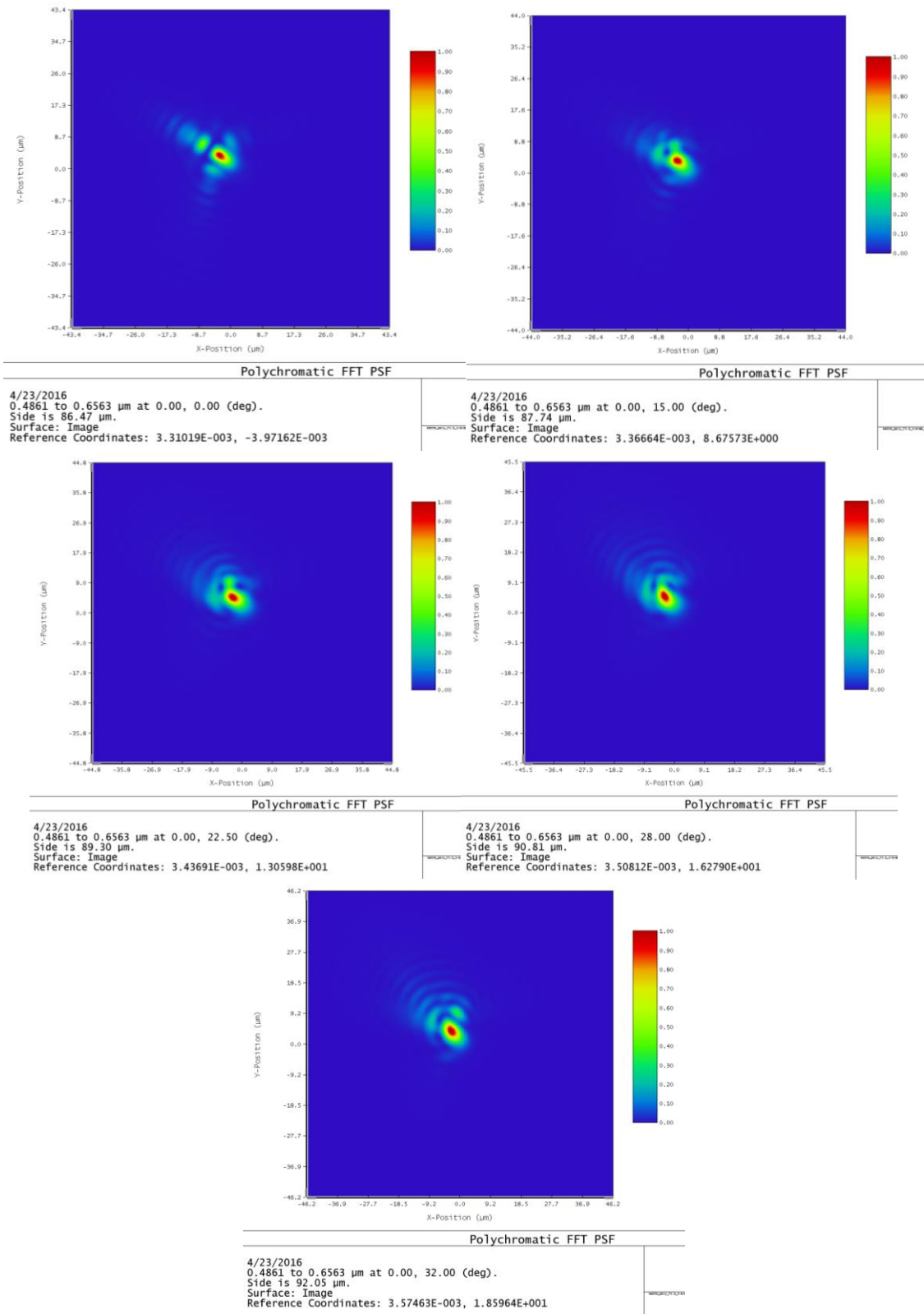


Figure 39 - Composite of diffraction PSFs for the field-invariant retrofocus lens for all five field angles.

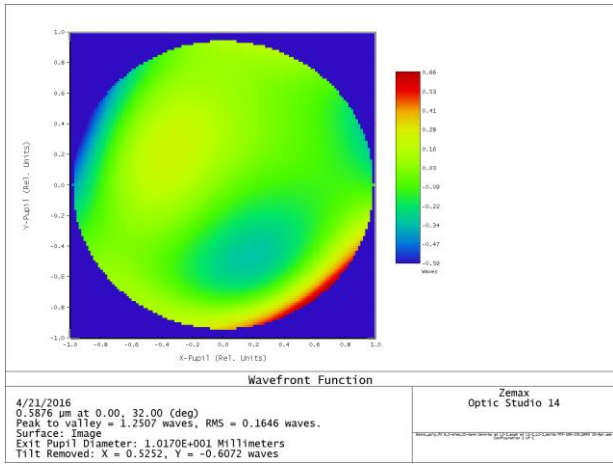
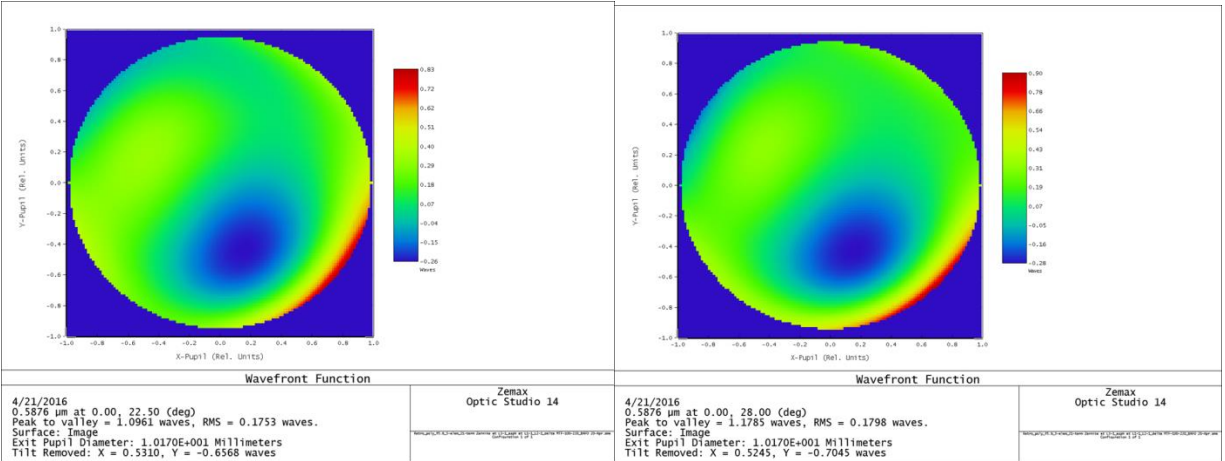
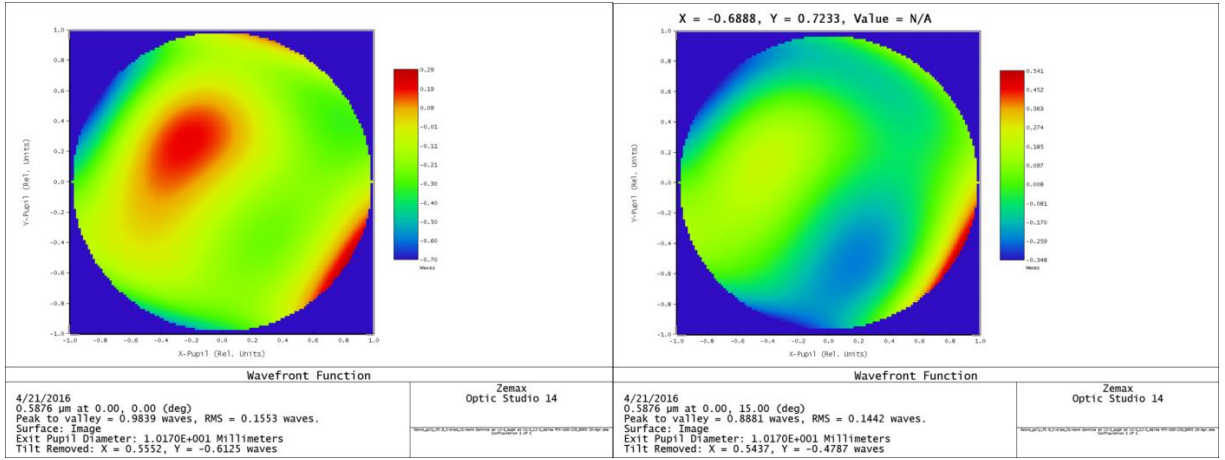


Figure 40 - Composite of exit pupil wavefront surface maps for the field-invariant retrofocus lens for all five field angles.

OPD plots (Figure 41) are shown, which underscore this lens's field invariance by similarity of shape and magnitude of the OPD plots at all field angles. Field curvature/distortion plots (Figure 42), and relative illumination plots (Figure 43) are also shown. While the 10% distortion at the full field is substantial, it is similar to that of the baseline lens. It is also worth noting that the relative illumination drops to 80% at full field, which contrasts with about 50% which would result from cosine-fourth fall-off if the exit and entrance pupils were the same size. Figure 44, which depicts the through-focus MTF for both the field-invariant lens and the baseline lens, gives us insight as to how the addition of the asymmetric asphere has helped enable field-invariance. By substantial increase of depth of focus in the field-invariant lens, we have obtained an expanded focus budget which relaxes the FC, astigmatism, and chromatic change of focus constraints on the lens design, which in turn allows the existing optical degrees of freedom to optimize primarily for other aberrations.

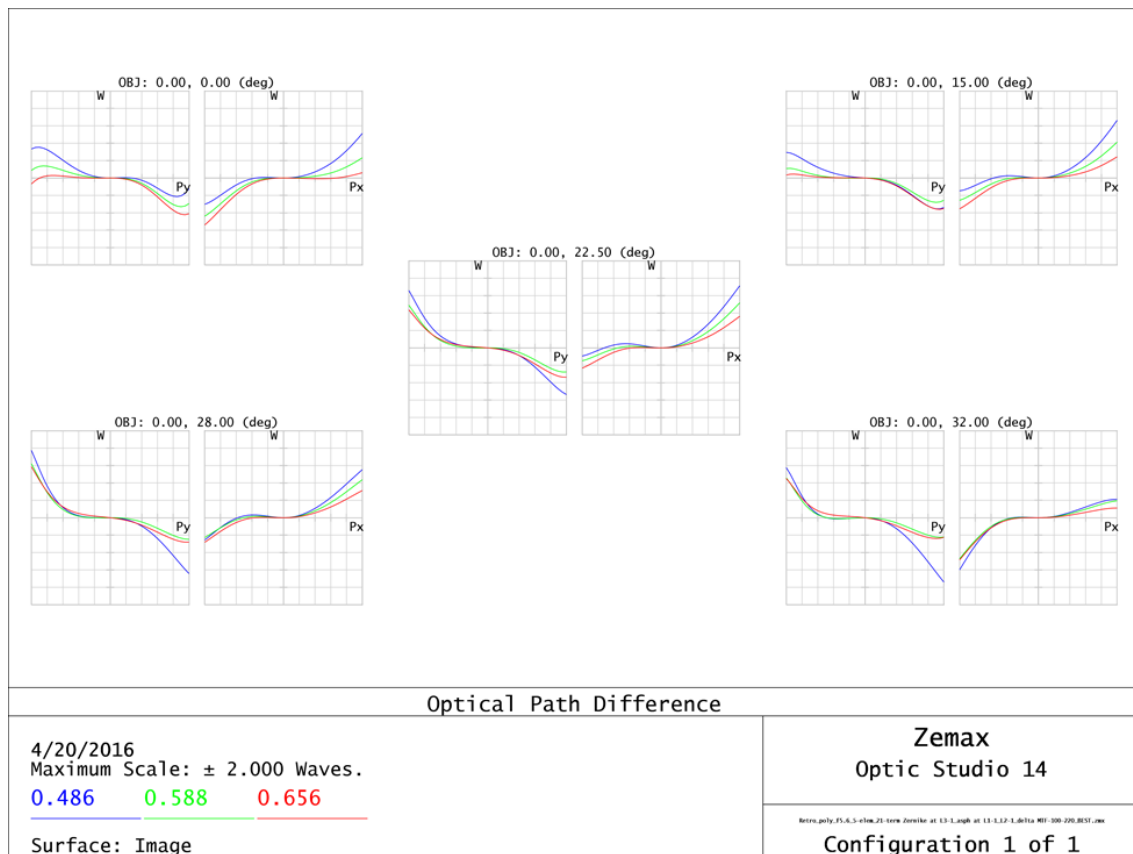


Figure 41 – Composite of OPD plots for the field-invariant retrofocus lens for all five field angles.

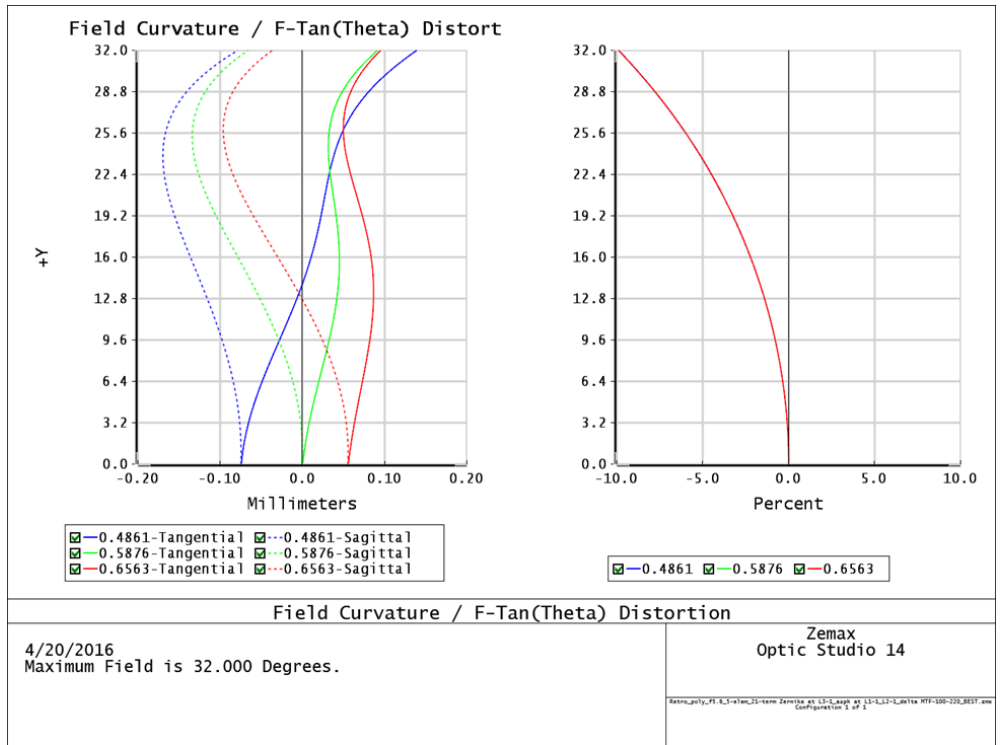


Figure 42 – Field curvature and distortion vs. field angle plots for the field-invariant retrofocus lens.

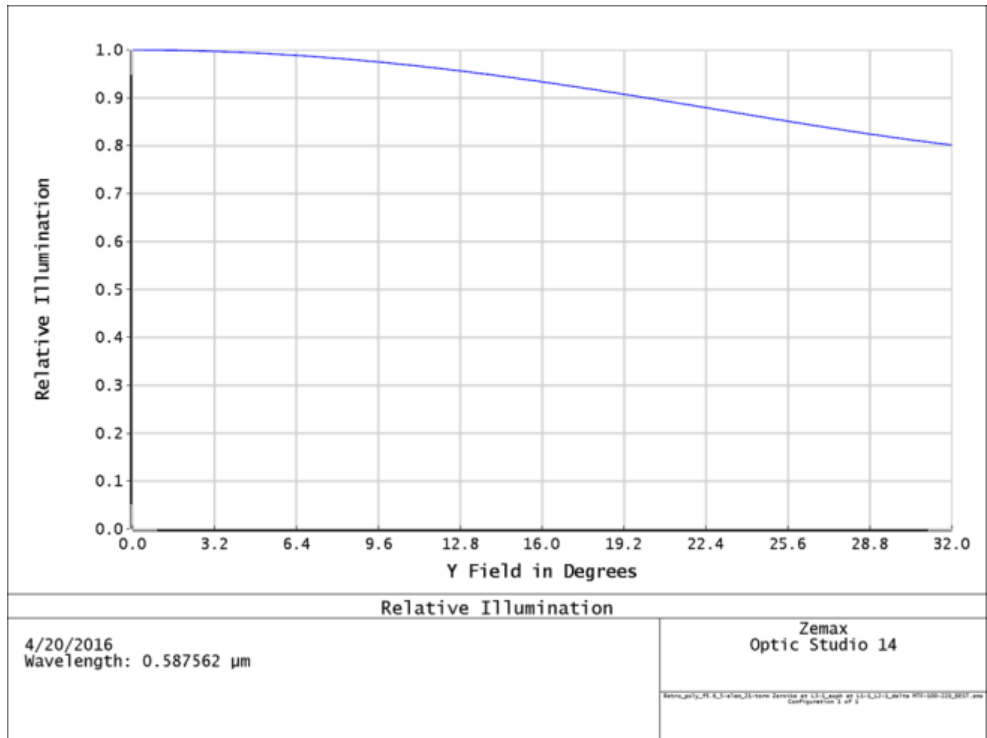


Figure 43 – Relative illumination plot vs. field angle for the field-invariant retrofocus lens.

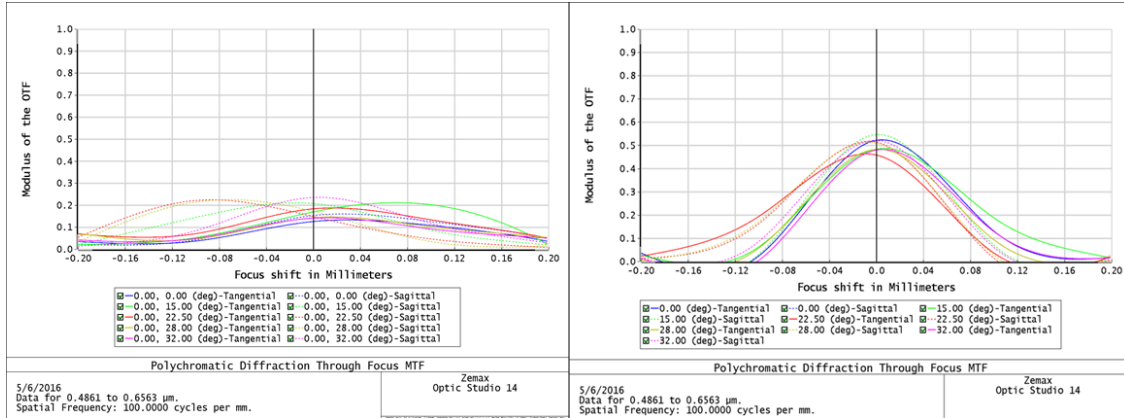


Figure 44 - Comparison of through-focus MTF for the field-invariant lens (left) and the baseline lens (right)

The final element counts by element type for the baseline lens and the field-invariant lens are summarized in Table 2. Because the total optical element count is reduced by two, a significant cost and weight reduction are achieved with the field-invariant lens design.

Lens Element Types	Baseline Lens	Field-invariant Lens
Spherical elements	4	2
Aspheric elements	3	3
Asphere #1	Even polynomial – 8 th order	Even polynomial – 8 th order
Asphere #2	Even polynomial – 6 th order	Even polynomial – 8 th order
Asphere #3	Even polynomial – 8 th order	Zernike polynomial – 21 st order
Total elements	7	5

Table 2 - Comparison of baseline and field-invariant retrofocus lenses.

Chapter 3 Digital Image Restoration

Having developed a 5-element WFOV lens with a nearly invariant MTF and PSF across the entire field, we need to quantify the full system level performance within the computational imaging framework. This implies the critical step of digital image restoration to produce image quality equivalent to that expected from the more complicated, but diffraction limited baseline lens. Image restoration is an extensively researched field that has evolved over many decades. However, the predominant choice is the classic Wiener filter – developed in the 1960s – when restoration in real-time drives the need for low complexity [12][40]. Prasad et al [10] also argue the advantages of direct Wiener filters over the more computationally intensive iterative filters for real-time applications. Adelsberger [20] reached the same conclusion much more recently when comparing Wiener filters with the non-linear Richardson-Lucy filter.

3.1.Linear Wiener filter design

The basic premise of the Wiener filter is based on the foundation of frequency domain PSF deconvolution by dividing the Fourier transform of a sensed image by the transfer function of the imaging system to reproduce the original object's Fourier transform. This is shown in equation (5), where G represents the sensed image, F represents the original object, and H represents the system transfer function in the Fourier domain. The variables u, v denote the spatial frequency variables corresponding to the x and y image dimensions:

$$G(u, v) = F(u, v) \cdot H(u, v) \Rightarrow F(u, v) = \frac{1}{H(u, v)} \cdot G(u, v) \quad (5)$$

The multiplier $\frac{1}{H(u, v)}$ in this equation is the inverse reconstruction filter. It is well-known, however, that measurement noise corrupts all electronic imagery, and when the transfer function $H(u, v)$ that corresponds to the optical MTF curve approaches zero, the filter gain increases indefinitely, amplifying noise present in $G(u, v)$ to such high levels in the reconstructed image as to make it

unusable. Thus a more sophisticated reconstruction filter is required, which leads to the Wiener filter. Since noise is generally an unknown quantity, perfect restoration of the original object is not plausible. Instead, our task is to produce the highest-confidence estimate of what the original object is, which is to say that we wish to minimize the average error between our estimate and the true object function. This is expressed as follows:

$$\min E \{ \|f - \hat{f}\|^2 \}, \quad (6)$$

where f represents the original object, and \hat{f} represents our reconstruction estimate. To achieve this best estimate, the Wiener filter incorporates the expected signal to noise ratio of the imager to limit the filter gain at the highest spatial frequencies where the strength of image noise may be comparable to that of true image content, while maintaining high gain similar to the inverse reconstruction filter at lower spatial frequencies. This leads to the following design of the Wiener filter [41]:

$$W(u, v) = \frac{H^*(u, v)}{|H(u, v)|^2 + \phi_n(u, v) / \phi_f(u, v)}, \quad (7)$$

where ϕ_n and ϕ_f represent the expected power spectra of the noise and original image, respectively. Figure 45 depicts a representative Wiener filter, with gain at lower spatial frequencies and attenuation at higher spatial frequencies to suppress noise. In the entire portion of the curve where the Wiener filter gain is greater than 1, noise will be amplified as well as signal, so it is desirable to minimize the gain required by maximizing the optical MTF.

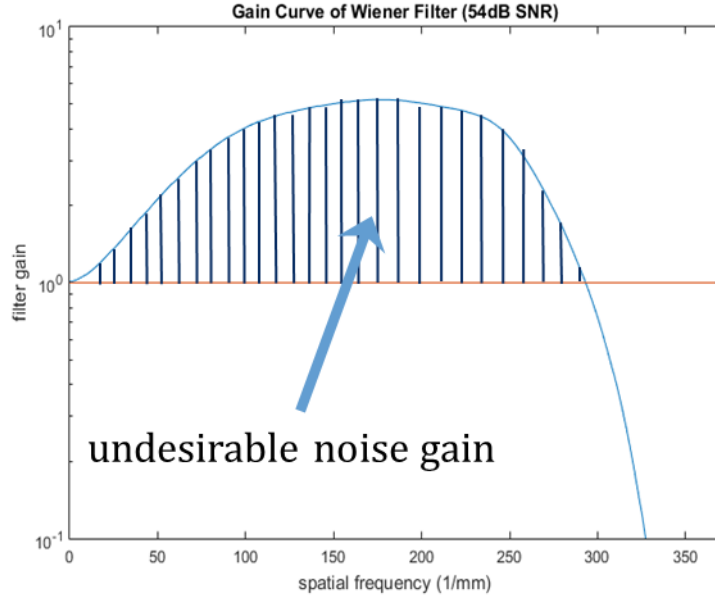


Figure 45 – Representative Wiener filter gain curve

When the expected noise power spectrum is zero, the Wiener filter degenerates to the exact form of equation (5). We can express the image reconstruction in the frequency domain as:

$$\hat{F}(u, v) = W(u, v) \cdot G(u, v) \quad (8)$$

Substituting equation (5) into equation (8), we obtain:

$$\hat{F}(u, v) = [W(u, v) \cdot H(u, v)] \cdot F(u, v) = STF(u, v) \cdot F(u, v) \quad (9)$$

Thus the full STF is the product of the Wiener filter function $W(u, v)$ and the pre-restoration transfer function $H(u, v)$, which is now assumed to include the optical MTF and measurement noise. The effect of this is shown in Figure 46, which depicts our field-invariant lens MTF and an STF which is the product of that MTF with a Wiener filter that is designed for it.

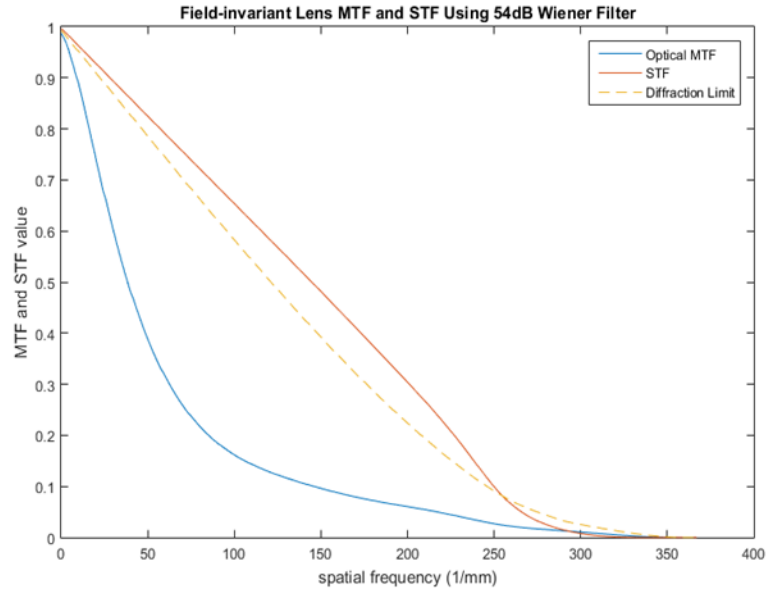


Figure 46 - MTF and STF curves.

In the following section we simulate the degradation of an object by our STFs via blurring and the addition of noise. We then simulate digital restoration of the image acquired from the field-invariant lens via Wiener filtering to obtain reconstructed images for comparison against the baseline lens.

3.2. Image simulation

Our present objective is to design a Wiener filter for use with the field-invariant retrofocus lens of Figure 33, and by employing it to deconvolve the PSF of that lens, achieve imaging performance equivalent to the raw imagery obtained from the diffraction limited baseline lens of Figure 17. But first we must produce simulated images which are representative of what might be physically produced by the two lenses respectively. Toward this end we choose a monochrome image of manageable size (512 x 512 x 8-bit) and level of detail to serve as our object, an old black and white photo of the Steward Observatory at the University of Arizona (Figure 47).

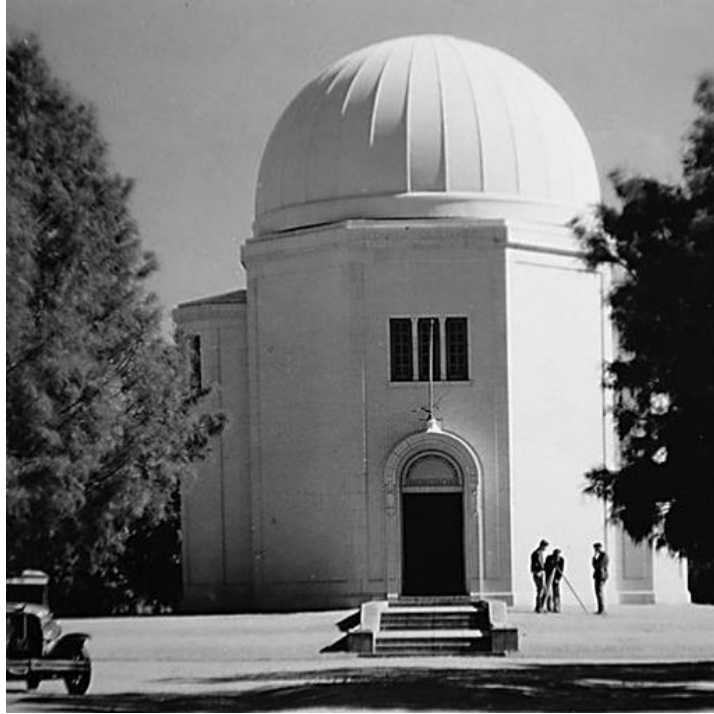


Figure 47 – Black and white photo of University of Arizona Steward Observatory used as object for image simulations.

For each of the two lenses, the test image was first passed through the OpticStudio™ model to simulate the optical distortion and relative illumination effects. The resulting images and the MTF curves for all five fields (both tangential and sagittal) were obtained from OpticStudio™, and the MTF data were averaged across all fields. The rationale for averaging MTF across all fields derives from the fact that fluctuations in MTF over the fields are small. Therefore the average MTF yields a good approximation to the actual field-dependent MTF in the real system. The images and averaged MTF curves were then imported to MATLAB® and the MTF curves subsequently resampled onto a 2D grid to match the 512x512 digital image geometry. A MATLAB® function was created to perform this resampling. The MTFs were then scaled 1/20X in the spatial frequency dimension to achieve a corresponding 20X reduction in the effective cutoff frequency. This scaling was necessary to enable spatial sampling at a scale smaller than the PSF. In the spatial frequency domain this means the scaling narrowed the lens MTF so that it is limiting the image quality rather than the narrow pixel MTF resulting from large pixels. We were then able to blur the images using MATLAB®'s built-in

FFT and inverse FFT functions by (a) 2D Fourier transforming the images, (b) pixel-wise multiplying the Fourier transforms by the MTF functions, and (c) inverse 2D Fourier transforming to achieve a blurred image. The results are shown in Figure 48 for the baseline and invariant lenses. We can easily observe some blurring effect of finite PSF size in terms of the baseline case and significantly more blurring in the invariant case.



Figure 48 – Image distorted and blurred by baseline lens (left) and invariant lens (right)

3.3. Digital image restoration and analysis

To perform restoration of the blurred image from the invariant lens, we needed to create a Wiener filter using equation (7). Since we have the MTF function $H(u, v)$, we need an estimate for the signal-to-noise ratio $\phi_n(u, v)/\phi_f(u, v)$ in order to design a filter. A Matlab® function, courtesy of Kerviche [42] is used for this analysis. Given that the image is 8-bit, we use 255 as the peak signal and use different noise levels as input estimates. Because ϕ_n and ϕ_f represent power spectra, the voltage-based image data – both signal and noise – need to be squared for input to the filter design. For example, if a noise standard deviation of 2 counts were expected in this 8-bit system, we would

input $\phi_n = 4.0$ and $\phi_f = 255^2 \cong 65000$. If the filter design function uses the SNR expressed in dB (as our function does), we calculate it as $SNR(dB) = 10\log(\phi_f/\phi_n)$. In the case above that would give us $10\log(65000/4) = 42dB$.

Once a Wiener filter has been designed, restoration of an image is a simple matter of (a) 2D Fourier transforming the degraded image, (b) pixel-wise multiplying the Fourier transform by the Wiener filter, and (c) inverse 2D Fourier transforming to achieve a restored image. Using this procedure on the blurred (but noiseless) image of Figure 48(right) at a SNR of 40dB, we obtain the restored image shown in Figure 49 side by side with the image blurred by the baseline lens. Comparing these images we observe that the two are nearly indistinguishable.

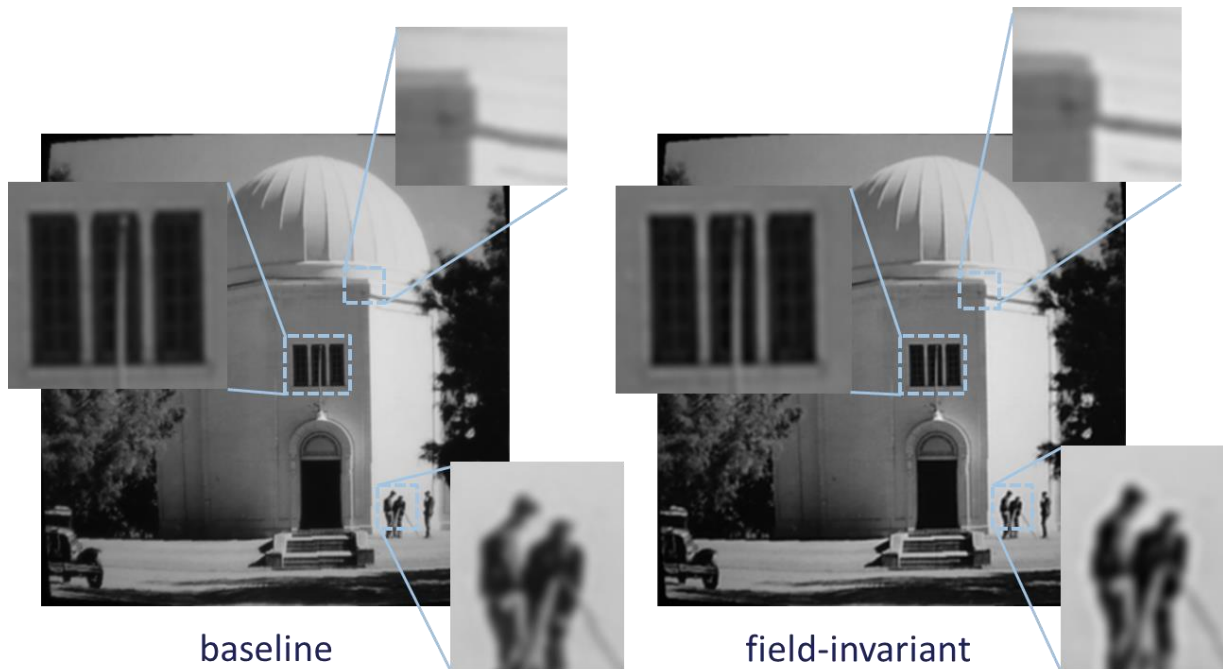


Figure 49 – Baseline raw image (left) and restored image from invariant lens (right)

To test the Wiener filter’s ability to minimize noise amplification, we use Matlab® to generate random, zero-mean, Gaussian noise of a desired standard deviation and add it to our image. The Wiener filter designed above uses 40dB as its SNR, which corresponds to a noise standard deviation of 2.5 digital counts. To visualize the effect of noise propagation through the Wiener filter, however, we start out by

adding a lower noise level of 1.0 count standard deviation ($\sim 0.4\%$ of the full 8-bit dynamic range) to our original blurred image and then passing it through the Wiener filter. This yields the restored image shown in Figure 50 (right). For comparison, Figure 50 (left) shows the blurred baseline image with the same level of noise added. The images are very similar in appearance, suggesting that the Wiener filter has successfully restored the image with sufficient high-frequency roll-off to avoid significant noise amplification.

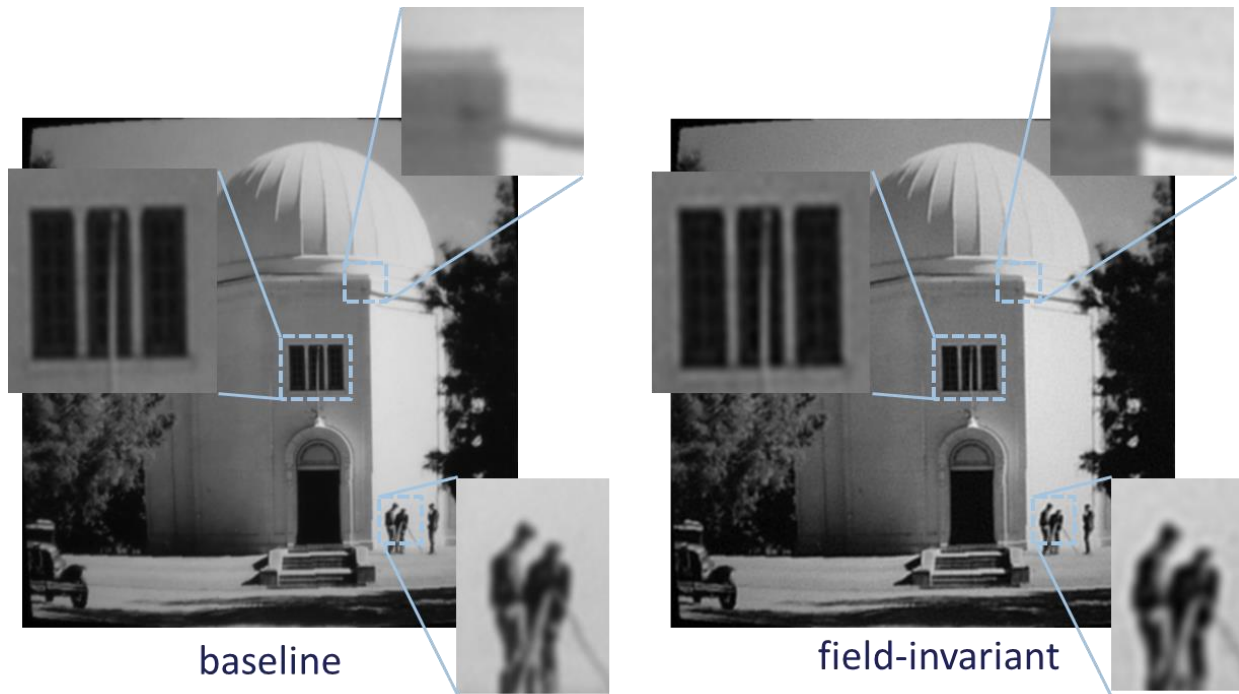


Figure 50 – Baseline lens image with noise std dev = 0.4% of dynamic range (48dB) added (left), and restored invariant image with noise std dev = 0.4%

To test the image restoration using the Wiener filter at higher noise levels, we increase the measurement noise to 4.0 digital counts standard deviation, or $\sim 1.6\%$ of the dynamic range. This corresponds to a measurement SNR of 36dB, which was the lowest we could use for the Wiener filter design and still get image edge sharpness comparable to the baseline lens. The restored image of Figure 51 (right) is shown side by side with the baseline noisy image. As we can see, the restored invariant image is visibly noisier than its baseline comparison image with the same level of measurement noise added. Thus we conclude that the limited modulation depth available from the field-invariant lens at high

frequencies limits the system to measurement noise standard deviation lower than about 1.6% of full range, with the precise limit falling between 0.4% and 1.6% of full range.

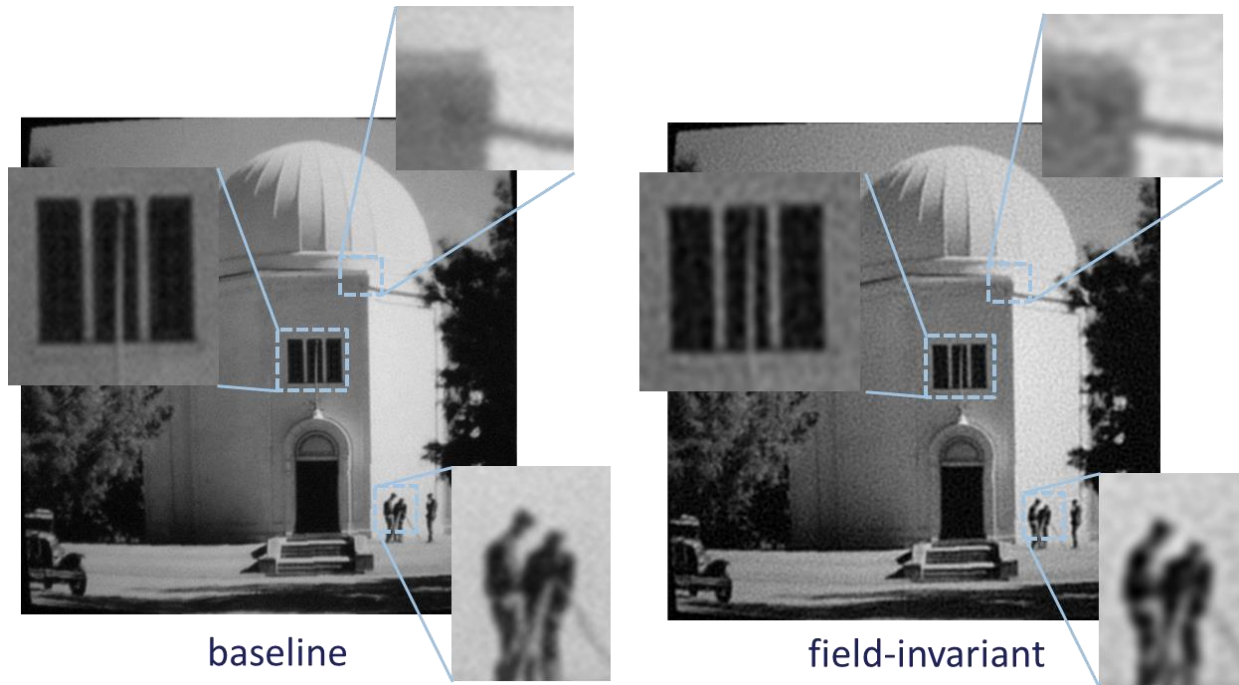


Figure 51 - Baseline lens image with noise std dev = 1.6% of dynamic range (36dB) added (left), and restored invariant image with noise std dev = 1.6%

Chapter 4 Conclusion and Future Work

Several wide FOV lens design forms were explored as candidates for a computational imager design with lower optical complexity that achieves near diffraction-limited performance over the full field. The retrofocus lens type was found to be the most suitable design form for this objective, primarily due to the advantage that its innate exit pupil magnification reduces the obliquity of off-axis light through the aperture stop and thus supports a higher cutoff frequency at those fields.

A candidate field-invariant retrofocus-style lens and a comparable baseline lens with two more lens elements were designed and optimized, each with three aspheric surfaces. We found that inclusion of an odd aspheric (not radially symmetric) surface was an essential enabling factor to achieve reasonable MTF performance at high spatial frequencies. This is perhaps not surprising because defocus is known for inducing zeroes in MTF at higher spatial frequencies, and asymmetric phase plates have been established as a means to mitigate focus-related aberrations in lenses ([1][2][4]).

Using Matlab® based simulations we were able to demonstrate that digital image restoration using Wiener filters was able to fully restore the imagery from the field-invariant lens with reasonable noise levels. High levels of noise, however, degraded the final image quality so that it was untenable to achieve equivalent performance to that of the baseline diffraction-limited lens in that regime.

Use of an asymmetric aspheric surface in the lens design was employed as a last design degree of freedom to ensure our design objectives were met. As such, there is opportunity for additional work in the areas of cost-optimizing the aspheric surfaces, including researching where cost breakpoints may exist in the CNC optical fabrication community and the optical shop testing community. Furthermore, we believe that higher order odd aspherics (e.g. 7th radial order terms) may offer further improvement in system performance – potentially with even fewer optical elements, based on similar success for EDoF design in [12]. Further work would also involve tolerancing of the lens design to ensure the aspherics – and the asymmetric asphere in particular – are not driving unusual alignment precision.

References

- [1] E. R. Dowski and W. T. Cathey, "Extended depth of field through wave-front coding," *Appl. Opt.* 34, 1859-1866 (1995)
- [2] W. T. Cathey and E. R. Dowski, "New paradigm for imaging systems," *Appl. Opt.* 41, 6080-6092 (2002)
- [3] R. C. Gonzalez, R. E. Woods, and S. L. Eddins, *Digital Image Processing Using MATLAB®*. 2nd Ed. (Gatesmark Publishing, 2009), Chap. 5.
- [4] K. Kubala, E. Dowski, and W. T. Cathey, "Reducing complexity in computational imaging systems," *Opt. Express* 11, 2102-2108 (2003)
- [5] G. E. Johnson; A. K. Macon; G. M. Rauker; "Computational imaging design tools and methods." *Proc. SPIE 5524, Novel Optical Systems Design and Optimization VII*, 284 (October 22, 2004)
- [6] P. Y. Maeda ; P. B. Catrysse ; B. A. Wandell; "Integrating lens design with digital camera simulation." *Proc. SPIE 5678, Digital Photography*, 48 (April 04, 2005)
- [7] D. Robinson and D. G. Stork, "Joint Design of Lens Systems and Digital Image Processing," in *International Optical Design*, Technical Digest (CD) (Optical Society of America, 2006), paper WB4.
- [8] D. G. Stork and M. D. Robinson, "Theoretical foundations for joint digital-optical analysis of electro-optical imaging systems," *Appl. Opt.* 47, B64-B75 (2008)
- [9] A. Castro and J. Ojeda-Castañeda, "Asymmetric phase masks for extended depth of field," *Appl. Opt.* 43, 3474-3479 (2004)
- [10] S. Prasad ; T. C. Torgersen ; V. P. Pauca ; R. J. Plemmons ; J. van der Gracht; "Engineering the pupil phase to improve image quality." *Proc. SPIE 5108, Visual Information Processing XII*, 1 (August 11, 2003)

- [11] O. Palillero-Sandoval, J. F. Aguilar, and L. R. Berriel-Valdos, "Phase mask coded with the superposition of four Zernike polynomials for extending the depth of field in an imaging system," *Appl. Opt.* 53, 4033-4038 (2014)
- [12] R. Kerviche and A. Ashok, "A Joint-Design Approach for Extended Depth of Field Imaging," in *Imaging and Applied Optics*, OSA Technical Digest (online) (Optical Society of America, 2013), paper CW4C.4.
- [13] C. Dorronsoro ; J. A. Guerrero-Colon ; M. C. de la Fuente ; J. M. Infante ; J. Portilla; "Low-cost wavefront coding using coma and a denoising-based deconvolution." *Proc. SPIE 6737*, Electro-Optical and Infrared Systems: Technology and Applications IV, 67370E (October 08, 2007)
- [14] M. D. Robinson and D. G. Stork, "Joint digital-optical design of superresolution multiframe imaging systems," *Appl. Opt.* 47, B11-B20 (2008)
- [15] M. D. Robinson; D. G. Stork; "Joint digital-optical design of imaging systems for grayscale objects." *Proc. SPIE 7100*, Optical Design and Engineering III, 710011 (September 27, 2008)
- [16] Z. Liu, L. Tian, S. Liu, L. Waller; "Real-time brightfield, darkfield, and phase contrast imaging in a light-emitting diode array microscope." *J. Biomed. Opt.* 19(10), 106002 (Oct 01, 2014).
- [17] T. Nakamura, R. Horisaki, and J. Tanida, "Computational superposition compound eye imaging for extended depth-of-field and field-of-view," *Opt. Express* 20, 27482-27495 (2012)
- [18] V. Treeaporn, A. Ashok, and M. A. Neifeld, "Increased Field of View through Optical Multiplexing," in *Imaging Systems*, OSA technical Digest (CD) (Optical Society of America, 2010), paper IMC4.
- [19] H. B. Wach, E. R. Dowski, and W. T. Cathey, "Control of chromatic focal shift through wavefront coding," *Appl. Opt.* 37, 5359-5367 (1998)
- [20] K. Adelsberger. "Design guidelines for wavefront coding in broadband optical systems." ProQuest Dissertations and Theses. Order No. 3614827. University of Rochester (2014).

- [21] F. E. Sahin, P. J. Nasiatka, and A. R. Tanguay, “Lateral Chromatic Aberration Optimization in Wide-Field-of-View Computational Cameras,” in *Frontiers in Optics 2015*, OSA Technical Digest (online) (Optical Society of America, 2015), paper FTh1F.4.
- [22] D. Shafer; “Lens designs with extreme image quality features.” *Advanced Optical Technologies*. Volume 2, Issue 1, Pages 53–62, February 2013
- [23] K. P. Thompson; J. P. Rolland; “Will computational imaging change lens design?” *Proc. SPIE 9293*, International Optical Design Conference 2014, 929302 (December 17, 2014)
- [24] OpticStudio14 SP2 Professional (64-bit) May 2014. OpticStudio is a registered trademark of Zemax LLC, Kirkland, WA.
- [25] MATLAB® R2016a (9.0.0.341360) 64-bit (win64) February 2016. The MathWorks, Inc., Natick, MA.
- [26] K. E. Dalzell ; R. P. Jonas ; B. P. Wallace; “The use of low departure aspheric surfaces in high quality wide angle lenses.” *Proc. SPIE 9626*, Optical Systems Design 2015: Optical Design and Engineering VI, 96261F (September 23, 2015)
- [27] S. Mezouari; Andrew R. Harvey; “Primary aberrations alleviated with phase pupil filters.” *Proc. SPIE 4768*, Novel Optical Systems Design and Optimization V, 21 (September 5, 2002)
- [28] J. B. Caldwell; “Lens systems with large optical invariant.” *Proc. SPIE 5865*, Tribute to Warren Smith: A Legacy in Lens Design and Optical Engineering, 58650G (August 18, 2005)
- [29] W. J. Smith, *Modern Lens Design*, 2nd Ed. (McGraw-Hill, 2005), Chap. 2, p. 42.
- [30] J. Sasian; “From the landscape lens to the planar lens: a reflection on teaching lens design.” *Proc. SPIE 5865*, Tribute to Warren Smith: A Legacy in Lens Design and Optical Engineering, 58650I (August 18, 2005)
- [31] Homework assignment completed by the author from course OPTI 517, College of Optical Sciences, University of Arizona, 2015.
- [32] W. J. Smith, *Modern Lens Design*, 2nd Ed. (McGraw-Hill, 2005), Chap. 12, p. 332.
- [33] J. E. Grievenkamp, *Field Guide to Geometrical Optics* (SPIE Press, 2004), p. 29.

- [34] J. W. Goodman, *Introduction to Fourier Optics* (McGraw-Hill, 1968), Chap. 6, p. 119.
- [35] I. Mori, "Retrofocus-Type Lens System," US Patent #3,635,546.
- [36] W. J. Smith, *Modern Lens Design, 2nd Ed.* (McGraw-Hill, 2005), Chap. 14, pp. 402-403.
- [37] J. E. Grievenkamp, *Field Guide to Geometrical Optics* (SPIE Press, 2004), p. 89.
- [38] K. Momiyama, H. Yokota, "Wide angle photographic lens," US Patent #4,257,678.
- [39] R. J. Noll, "Zernike polynomials and atmospheric turbulence," *J. Opt. Soc. Am.*, Vol. 66, No. 3, 207-211 (1976).
- [40] M. R. Banham and A. K. Katsaggelos, "Digital image restoration," in *IEEE Signal Processing Magazine*, vol. 14, no. 2, pp. 24-41, Mar 1997.
- [41] L. R. Berriel, J. Bescos, and A. Santisteban, "Image restoration for a defocused optical system," *Appl. Opt.* 22, 2772-2780 (1983).
- [42] Wiener filter generation MATLAB® code developed by Ronan Kerviche, University of Arizona, 2016.
- [43] F. Heide, M. Rouf, M. B. Hullin, B. Labitzke, W. Heidrich, and A. Kolb, "High-quality computational imaging through simple lenses." *ACM Transactions on Graphics (TOG)* Volume 32 Issue 5, September 2013.